Adaptively implicit advection for atmospheric flows

JAMES | Journal of Advances in Modeling Earth Systems®

RESEARCH ARTICLE
10.1029/2024MS004503

Adaptively Implicit Advection for Atmospheric Flows

Hilary Weller[1], **Christian Kühnlein**[2], **and Piotr K. Smolarkiewicz**[3]

[1]Meteorology, University of Reading, Reading, UK, [2]ECMWF, Bonn, Germany, [3]NSF National Center for Atmospheric Research, Boulder, CO, USA

Key Points:

- Implicit time-stepping for advection enables large Courant numbers
- Implicit time-stepping for advection is cheap as it combines an explicit correction with a simple first-order accurate implicit estimate
- Implicit time-stepping enables monotonicity, conservation and unconditional stability

Correspondence to:
H. Weller,
h.weller@reading.ac.uk

Citation:
Weller, H., Kühnlein, C., & Smolarkiewicz, P. K. (2024). Adaptively implicit advection for atmospheric flows. *Journal of Advances in Modeling Earth Systems*, *16*, e2024MS004503. https://doi.org/10.1029/2024MS004503

Received 12 JUN 2024
Accepted 1 NOV 2024

Author Contributions:
Conceptualization: Hilary Weller, Christian Kühnlein, Piotr K. Smolarkiewicz
Data curation: Hilary Weller
Formal analysis: Hilary Weller
Investigation: Hilary Weller
Methodology: Hilary Weller, Christian Kühnlein, Piotr K. Smolarkiewicz
Resources: Hilary Weller
Software: Hilary Weller
Validation: Hilary Weller
Visualization: Hilary Weller
Writing – original draft: Hilary Weller
Writing – review & editing: Hilary Weller, Christian Kühnlein, Piotr K. Smolarkiewicz

Abstract Implicit time-stepping for advection is applied locally in space and time where Courant numbers are large, but standard explicit time-stepping is used for the remaining solution which is typically the majority. This adaptively implicit advection scheme facilitates efficient and robust integrations with long time-steps while having negligible impact on the overall accuracy, and achieving monotonicity and local conservation on general meshes. A novel and important aspect for the efficiency of the approach is that only one iteration is needed each time the linear equation solver is called for solving the advection equation. The demonstration in this paper uses the second-order Runge-Kutta implicit/explicit time integration in combination with a second/third-order finite-volume spatial discretization and is tested using deformation flow tracer advection on the sphere and a fully compressible model for atmospheric flows. Tracers are advected over the poles of highly anisotropic latitude-longitude grids with very large Courant numbers and on quasi-uniform hexagonal and cubed-sphere meshes with the same algorithm. Buoyant flow simulations with strong local updrafts also benefit from adaptively implicit advection. Stably stratified compressible flow simulations require a stable combination of implicit treatment of gravity and acoustic waves as well as advection in order to achieve long time-steps.

Plain Language Summary Weather and climate prediction models take small time-steps in order to make predictions about the future, starting from estimates of current conditions. The smaller the time-steps are, the more of them have to be taken to make a prediction for a given time in the future. The more time-steps that have to be taken, the more expensive the prediction is. If the time-steps are too big, models can not only lose accuracy, they can become unstable—inaccuracies can become so large that wild oscillations are generated and the model crashes. These instabilities are often caused by the advective transport of constituents of the atmosphere by the wind. This paper describes a method—adaptive implicit advection—for calculating atmospheric transport using longer time-steps while maintaining stability. We show that this can be achieved with minimal additional cost, and accuracy is only lost locally, where the time-step is large relative to the flow speed and model grid size.

1. Introduction

Weather and climate models can have severe time-step restrictions due to advection (e.g., Cullen & Davies, 1991; Dennis et al., 2012; Giraldo et al., 2013; Kühnlein et al., 2019; Melvin et al., 2019). Historically these were most problematic near the poles of latitude-longitude grids, and could be circumvented using techniques such as polar filtering (Cullen & Davies, 1991) and semi-Lagrangian advection (Davies et al., 2005; Hortal, 2002; Pudykiewicz & Staniforth, 1984; Purser & Leslie, 1991; Robert, 1982; P. K. Smolarkiewicz & Rasch, 1991). State-of-the-art atmospheric models have moved away from full latitude-longitude grids (e.g., Dennis et al., 2012; Giraldo et al., 2013; Kühnlein et al., 2019; Melvin et al., 2019) but models that use explicit Eulerian schemes for advection still have significant time-step restrictions where high velocities occur and coincide with small spatial grid increments, for example, in storms, convection, jets, and in interaction with the underlying terrain.

Semi-Lagrangian advection is the most common approach to address time-step limitations. However, for the typical interpolating semi-Lagrangian schemes, this occurs at the expense of conservation. Semi-Lagrangian schemes are most straightforward to implement on structured grids, such as the latitude-longitude grid. Nevertheless, efficient advective-form (i.e., non-conservative) algorithms that allow very long time-steps have been developed for the quasi-uniform octahedral grid in ECMWF's operational IFS (Diamantakis & Váňa, 2022; Malardel et al., 2016).

Conservative, cell-integrated, or flux-form semi-Lagrangian (FFSL) schemes (e.g., Lauritzen, 2007; Lin & Rood, 1996; Zerroukat et al., 2004) entail mapping the old time-step solution onto non-overlapping departure

cells (rather than interpolating onto departure points). This carries additional cost and complexity but enables long time-steps without sacrificing conservation. FFSL entails calculating fluxes of the quantity advected through faces each time-step. It can be made equivalent to cell-integrated semi-Lagrangian scheme for small Courant numbers (Lauritzen et al., 2011). For large Courant numbers, the swept volumes pass through multiple cells and the contribution from each cell is accounted for, leading to a cost that scales with Courant number. On structured grids this cost can be small (Leonard et al., 1995, 1996; Lin & Rood, 1996) and accuracy is retained for large time-steps (Chen et al., 2017). In practice, FFSL schemes are often used with small Courant numbers (Harris et al., 2011; Lauritzen et al., 2014; Lipscomb & Ringler, 2005; Miura, 2007; Putman & Lin, 2007; Skamarock & Menchaca, 2010) but the technique is being actively investigated by the UK Met Office for use with large Courant numbers on a cubed-sphere grid with promising results (Bendall & Kent, 2024).

Implicit time-stepping for advection has been used in computational fluid dynamics for decades (e.g., Yee & Harten, 1987) and is gaining popularity in atmosphere and ocean models (e.g., Baldauf et al., 2011; Jebens et al., 2011; Li & Dong, 2024; Shchepetkin, 2015; Weller et al., 2023; Wicker & Skamarock, 2020). There are some commonly held beliefs within atmospheric modeling about implicit time-stepping for advection that warrant further investigation:

1. Implicit time-stepping for advection is not worth the significant cost of the additional linear equation solutions. In particular, the additional linear equation solutions will entail a cost proportional to the time-step, implying that sub-steps for advection, or just smaller time-steps, would be more cost effective.
2. Additional implicit time-stepping schemes will reduce parallel scaling performance.
3. Implicit time-stepping entails severe advection phase errors.

There is also a mathematical order barrier which states that no implicit method exists which is monotonic for all time-steps and has order of accuracy greater than one in time (Gottlieb et al., 2001). Therefore, to create useful implicit method for advection, it is necessary to either drop the need for strict monotonicity (Yee & Harten, 1987) or downgrade to first-order accuracy where Courant numbers are large, which can be done using implicit extensions of flux-corrected transport (FCT, May & Berger, 2017; Weller et al., 2023).

This paper builds on Weller et al. (2023) (WWKS23) which created an adaptive implicit version of MPDATA (P. Smolarkiewicz & Margolin, 1998; P. Smolarkiewicz & Szmelter, 2005), which enabled arbitrarily large Courant numbers and was tested on deformational flow on a variety of meshes of the sphere, including with Courant numbers up to 70 over the pole of a rotated latitude-longitude grid. WWKS23 used two complementary types of adaptivity: (a) implicit advection only where the Courant number was above one, (b) the spatial and temporal order of accuracy gradually reduced to one for Courant numbers above one. Accuracy greater than first-order was achieved using explicit corrections, so the linear equation systems were sparse and diagonally dominant. There were shortcomings of this work:

- The stabilization necessary for large Courant numbers was stronger than predicted by theory.
- Number of matrix equation solver iterations scaled close to linearly with the domain mean Courant number.
- Only linear advection test cases in two spatial dimensions were presented.

In this paper we present an advection scheme with the following properties, which are assumed sufficient when the Courant number is only above one in small regions of the atmosphere:

- Accuracy and cost comparable with explicit time-stepping where the Courant number is less than one.
- Stable and at least first-order accurate for Courant numbers larger than one.
- Monotone for all Courant numbers (no spurious extrema generated).
- Suitable for quasi-uniform meshes of the sphere, unstructured meshes and meshes with local adaptivity.
- Exactly locally conservative.
- Some shared calculations between different advected species, enabling some multi-tracer efficiency.
- Theoretically good parallel scalability (not yet tested).
- Coupled with a solution of the Navier-Stokes equations with implicit treatment of acoustic and gravity waves.

This is achieved by using method-of-lines (Runge-Kutta) adaptively implicit time-stepping with a quasi-cubic upwind spatial discretization of advection terms coupled to a co-located (A-grid), second-order, finite volume

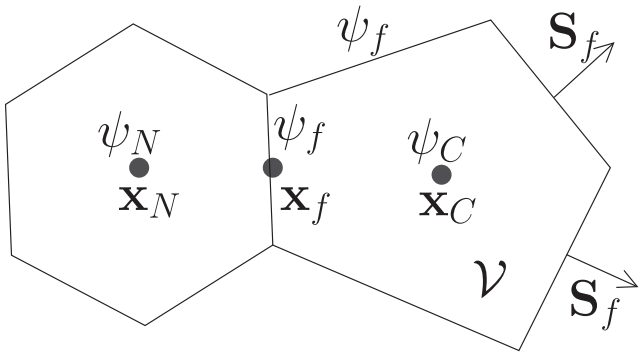

Figure 1. Cell C, with neighbor N, straddling face f in an arbitrary mesh. Cells have centers $\mathbf{x}_C$ and $\mathbf{x}_N$ and face f has center $\mathbf{x}_f$. Cell center quantity ψ has value ψ_f at the face. Cells have volume $\mathcal{V}$. Faces have area vectors $\mathbf{S}_f$ normal to the face with magnitude equal to the face area.

Navier-Stokes solver. We use a segregated, un-split approach between advection and other terms; the advection terms of the momentum and potential temperature equations are treated implicitly (where needed) while terms involving acoustic and gravity wave propagation are held fixed. Next, the advection terms are held fixed while acoustic and gravity waves are treated implicitly for the solution of the Helmholtz (pressure) equation. Outer iterations are necessary for convergence. The method-of-lines advection scheme is described in Section 2.2. The linear stability of the advection scheme with implicit treatment of gravity waves is analysed in Section 2.3. The coupling of the adaptively implicit advection with the Navier-Stokes equations is described in Section 2.4 and Appendix C. The spatial discretization has some novel aspects, some established methods and some imperfections. However spatial discretization is peripheral to the main topic of the paper, which is adaptive implicit advection, so the imperfections in the spatial discretization are not considered show stoppers. All numerical schemes are implemented and tested in the OpenFOAM 11C++ toolbox (OpenFOAM, accessed 2024). A range of standard test cases show that with adaptively implicit time-stepping, larger time-steps can be taken with minimal impact on accuracy and a consequent dramatic reduction in cost. Deformational flow linear advection test cases on the sphere are presented in Section 3.1, demonstrating that the method-of-lines scheme has improved performance to the implicit MPDATA of WWKS23. Section 3.2 shows results of buoyancy driven flows and Section 3.2 shows results of stably stratified flow over orography. These tests show the benefit of implicit treatment of gravity waves as well as acoustic waves and advection. Conclusions are drawn in Section 4.

2. Numerical Modeling

The discretization for advection and for other terms in the Navier-Stokes equations is split in space and time so that the PDEs are converted to ODEs using the spatial discretization described in Appendix B and Section 2.1. The ODEs are then solved with an implicit/explicit (IMEX) Runge-Kutta scheme with adaptively implicit advection (Section 2.2). The application of this scheme to the linear advection equation is described in Section 2.2.2 and to the Navier-Stokes equations in Section 2.4 and Appendix C. The presented time integration technique should be applicable with any spatial discretization.

The stability of the adaptive implicit advection coupled with implicit treatment of gravity waves is analysed in Section 2.3. This analysis is used to define (a) the parameter α that controls off-centering between old and new time levels, (b) flag β that controls implicit advection and (c) limiter γ that controls the higher-order spatial correction. A summary of the notation is given in Appendix A.

2.1. Quasi-Cubic Upwind Advection

This section describes a quasi-cubic advection scheme as implemented using OpenFOAM operators (OpenFOAM, accessed 2024). Some general description of OpenFOAM spatial discretization is in Appendix B.

Figure 1 shows a cell with value ψ_C at cell C and ψ_N at a neighbor cell N, with face f in between. Cells have volume $\mathcal{V}$ and faces have outward pointing area vectors $\mathbf{S}_f$ which are normal to the face with magnitude equal to the face area.

Divergence is calculated in cells with volume $\mathcal{V}$ using Gauss's theorem

$$\nabla \cdot \rho \mathbf{u} \psi \approx \frac{1}{\mathcal{V}} \int_{\mathcal{V}} \nabla \cdot \rho \mathbf{u} \psi \, \mathrm{d}\mathcal{V} = \frac{1}{\mathcal{V}} \int_{S} \psi \rho \mathbf{u} \cdot \mathrm{d}\mathbf{S} \approx \frac{1}{\mathcal{V}} \sum_{\text{faces}} \phi \psi_f, \tag{1}$$

where ρ is the fluid density, $\mathbf{u}$ is the velocity vector and ϕ is the mass flux through face f given as

$$\phi = \rho_f \mathbf{u}_f \cdot \mathbf{S}_f. \tag{2}$$

Quasi third-order accurate advection is implemented as a correction to the first-order upwind scheme defined as a blend, b, of two gradients

$$\psi_f = \underbrace{\psi_u}_{\text{1st order upwind}} + \underbrace{\gamma(\mathbf{x}_f - \mathbf{x}_u)\cdot\left(b\nabla_u\psi + (1-b)\nabla_f\psi\right)}_{\sim\text{3rd order correction (HOC)}}, \tag{3}$$

where

$$\text{the upwind cell, } u = \begin{cases} N & \text{if } \phi > 0 \\ C & \text{otherwise,} \end{cases} \tag{4}$$

$$\text{the downwind cell, } d = \begin{cases} N & \text{if } \phi \le 0 \\ C & \text{otherwise,} \end{cases} \tag{5}$$

where $\nabla_u\psi$ is the cell center gradient in cell u, defined in Equation B1, and $\nabla_f\psi$ is the gradient at the face, defined in Equation B4. The parameter $\gamma \in (0, 1]$ is the higher-order flux limiter (defined in Section 2.3). We assume that a blend, b, can be found to give third-order accuracy in representing $\partial\psi/\partial x$ on a one-dimensional, uniform grid. There will inevitably be errors on other grids. To find b, we assume that the uniform grid is indexed by j so that $\psi_j = \psi_u$ and $\psi_{j+1} = \psi_d$ for $u > 0$. It can be shown that the following approximation is third-order accurate on a uniform grid

$$\frac{\partial\psi}{\partial x_j} \approx \frac{2\psi_{j+1} + 3\psi_j - 6\psi_{j-1} + \psi_{j-2}}{6\Delta x}. \tag{6}$$

We express this as a difference between face values as

$$\frac{\partial\psi}{\partial x_j} = \frac{\psi_{j+\frac{1}{2}} - \psi_{j-\frac{1}{2}}}{\Delta x} \Rightarrow \psi_{j+\frac{1}{2}} = \frac{2\psi_{j+1} + 5\psi_j - \psi_{j-1}}{6}. \tag{7}$$

In Equation 3 the 3rd-order correction (high-order correction, HOC) is expressed as a linear combination of gradients. On a one-dimensional, uniform grid, these gradients are given as

$$\nabla_u\psi = \frac{\psi_{j+1} - \psi_{j-1}}{2\Delta x},\ \nabla_f\psi = \frac{\psi_{j+1} - \psi_j}{\Delta x} \text{ and } \mathbf{x}_f - \mathbf{x}_u = \frac{\Delta x}{2}.$$

Substituting these into Equation 3 gives

$$\begin{aligned} \frac{2\psi_{j+1} + 5\psi_j - \psi_{j-1}}{6} &= \psi_j + \frac{\Delta x}{2}\left(b\,\frac{\psi_{j+1} - \psi_{j-1}}{2\Delta x} + (1-b)\,\frac{\psi_{j+1} - \psi_j}{\Delta x}\right), \\ \Rightarrow b &= \frac{2}{3}. \end{aligned} \tag{8}$$

The parameter $b = \frac{2}{3}$ is then used for arbitrary two- and three-dimensional meshes in Equation 3, which provides third-order accuracy for $\gamma = 1$ in highly idealized settings when the meshes are uniform, as verified in Appendix D.

2.2. Adaptive Implicit Time-Stepping for Advection-Diffusion

2.2.1. Trapezoidal Implicit/Explicit

We first describe the solution of the ordinary differential equation

$$\frac{d\mathbf{y}}{dy} = L\mathbf{y} + N(\mathbf{y}) \tag{9}$$

for unknown $\mathbf{y}$ with a trapezoidal implicit/explicit scheme, where L is an invertible linear operator and $N(\mathbf{y})$ will be solved explicitly. The two-stage implicit/explicit trapezoidal scheme is

$$\frac{\mathbf{y}^k - \mathbf{y}^{(n)}}{\Delta t} = (1-\alpha)L\mathbf{y}^{(n)} + (1-\alpha)N\left(\mathbf{y}^{(n)}\right) + \alpha L\mathbf{y}^k + \alpha N\left(\mathbf{y}^{k-1}\right) \quad \text{for } k = 1,2, \text{ with } \mathbf{y}^{k=0} = \mathbf{y}^{(n)} \text{ and } \mathbf{y}^{(n+1)} = \mathbf{y}^{k=2}. \tag{10}$$

For $\alpha = 1/2$, this scheme is second-order accurate, being a combination of Crank-Nicolson and the explicit Heun/RK2 scheme. This scheme cannot be applied directly to the advection-diffusion scheme because α varies in space and so, for conservation, α must be inside all divergences.

2.2.2. Adaptively Implicit Runge-Kutta Applied to Advection-Diffusion

The adaptively implicit time-stepping provides a solution of the linear advection-diffusion equation

$$\frac{\partial \rho\psi}{\partial t} + \nabla\cdot\rho\mathbf{u}\psi - \nabla\cdot(\rho K\nabla\psi) = S_\psi, \tag{11}$$

for transported quantity ψ, where ρ is the density, $\mathbf{u}$ is the velocity vector and K the diffusion coefficient, while S_ψ subsumes source terms. In order to adapt the trapezoidal implicit/explicit scheme Equation 10 to solve Equation 11, we assume

$$\alpha L\mathbf{y} = -\nabla\cdot\left(\alpha\beta\rho\mathbf{u}\psi_{1\text{st}}\right) + \nabla\cdot(\alpha\rho K\nabla_2\psi), \tag{12}$$

$$\alpha N(\mathbf{y}) = -\nabla\cdot\left(\alpha(1-\beta)\rho\mathbf{u}\psi_{\text{HO}}\right) - \nabla\cdot\left(\alpha\beta\rho\mathbf{u}\psi_{\text{HOC}}\right) + \nabla\cdot(\alpha\rho K\nabla_{\text{noc}}\psi) + \alpha S_\psi, \tag{13}$$

where $\beta = 1$ selects implicit advection, $\psi_{1\text{st}}$ is the first-order approximation for ψ in the advection term and ψ_{HOC} is the high-order correction so that

$$\psi_{\text{HO}} = \psi_{1\text{st}} + \gamma\psi_{\text{HOC}}. \tag{14}$$

The symbol ∇_2 is the two-point difference for the normal gradient at a face and ∇_{noc} is the non-orthogonal correction (see Appendix B).

For $\psi = \mathbf{u}$, the corresponding source $S_\mathbf{u}$ contains the pressure gradient and gravity terms.

The mass flux and the density satisfy the mass continuity equation discretely which is given the shorthand

$$\frac{\partial\rho}{\partial t} = -\frac{1}{\mathcal{V}}\sum_{\text{faces}}\phi_f = -\nabla\cdot\phi. \tag{15}$$

In the description of the advection of ψ, the advecting velocity always appears with the density and it is always needed as a flux on faces. We therefore write the semi-discretized equations using the mass flux ϕ defined in Equation 2. To reduce the complexity of the presentation, ϕ can also symbolize a vector mass flux under the divergence operator.

Putting these together gives the adaptively implicit scheme with explicit high-order corrections

$$\begin{aligned}\frac{\rho^k\psi^k-\rho^{(n)}\psi^{(n)}}{\Delta t} = &- \nabla\cdot\left[(1-\alpha)\phi^{(n)}\psi^{(n)}_{\mathrm{HO}}\right]-\nabla\cdot\left[\alpha(1-\beta)\phi^{k-1}\psi^{k-1}_{\mathrm{HO}}\right]\\ &- \nabla\cdot\left[\alpha\beta\phi^{k-1}\psi^{k}_{\mathrm{1st}}\right]-\nabla\cdot\left[\alpha\beta\gamma\phi^{k-1}\psi^{k-1}_{\mathrm{HOC}}\right]\\ &+ \nabla\cdot\left[(1-\alpha)\rho_f K\nabla_S\psi^{(n)}\right]\\ &+ \nabla\cdot\left[\alpha\rho_f K\nabla_2\psi^{k}\right]+\nabla\cdot\left[\alpha\rho_f K\nabla_{\mathrm{noc}}\psi^{k-1}\right]\\ &+ (1-\alpha)\,S^{(n)}_{\psi}+\alpha S^{k-1}_{\psi}.\end{aligned} \tag{16}$$

This again uses the shorthand

$$\frac{1}{\mathcal{V}}\sum_{\mathrm{faces}}\phi\psi=\nabla\cdot\phi\psi. \tag{17}$$

The results in Section 3 use a maximum k of 2 (implying two outer iterations). In Equation 16, the mass fluxes are updated after ψ so the iteration count is $k-1$ for ϕ. This is explained in full in Appendix C. The implicit part of the time-stepping has commonality with Rosenbrock-W-methods (e.g., Rang & Angermann, 2005), but the possibility that $\alpha>1/2$ enables the scheme to be strong stability preserving (SSP, e.g., Pareschi & Russo, 2005) for large Courant numbers, which enables bounded solutions, avoiding the order barrier described by Gottlieb et al. (2001) by reverting to first-order accuracy.

Consistency with continuity will be addressed in Section C1.

2.2.3. Matrix Structure and Solution

The advection-diffusion Equation 16 is expressed as a matrix equation of the form

$$(A_\psi-H_\psi)\psi^k=R_\psi+T_\psi, \tag{18}$$

where A_ψ is a diagonal matrix, H_ψ is a matrix with zeros on the diagonal and R_ψ and T_ψ are the explicit right hand sides, consisting of all terms that do not depend on ψ^k. In order to calculate A_ψ and H_ψ we consider the first-order upwind discretization of $\nabla\cdot\alpha\beta\phi\psi$ at cell C with neighbors N

$$\begin{aligned}\nabla_{\mathrm{1st}}\cdot\alpha\beta\phi\psi &= \frac{1}{\mathcal{V}}\sum_{\phi\geq 0}\alpha\beta\phi\psi_C+\frac{1}{\mathcal{V}}\sum_{\phi<0}\alpha\beta\phi\psi_N\\ &= \frac{\psi_C}{\mathcal{V}}\sum_{\phi\geq 0}\alpha\beta\phi-\frac{1}{\mathcal{V}}\sum_{\phi<0}\alpha\beta|\phi|\psi_N,\end{aligned} \tag{19}$$

and the two-point discretization of the diffusion term

$$\nabla\cdot\left[\alpha\rho_f K\nabla_2\psi\right]=\frac{1}{\mathcal{V}}\sum_{\mathrm{faces}}\alpha\rho_f K\frac{\psi_N-\psi_C}{|\mathbf{d}_f|}|\mathbf{S}_f|. \tag{20}$$

Therefore A_ψ and H_ψ take the form

$$A_\psi=\frac{\rho^k}{\Delta t}+\frac{1}{\mathcal{V}_C}\sum_{\mathrm{faces}}\alpha\left(\beta\max(\phi,0)+\rho_f K\frac{|\mathbf{S}_f|}{|\mathbf{d}_f|}\right), \tag{21}$$

$$H_\psi(C,N)=\begin{cases}\dfrac{\alpha}{\mathcal{V}_C}\left(\beta\max(-\phi,0)+\rho_f K\dfrac{|\mathbf{S}_f|}{|\mathbf{d}_f|}\right) & \text{for row } C,\ \text{column } N\\ 0 & \text{otherwise,}\end{cases} \tag{22}$$

where α, β and ϕ are on face, f, between cells C and N. Note that:

- for inviscid flow ($K = 0$), or if K does not depend on ψ, then A_ψ and H_ψ do not depend on ψ,
- $A_\psi - H_\psi$ is diagonally dominant $\forall\ \alpha \geq 0, \beta \geq 0$.

The right hand side of Equation 18 contains the previous time-step, the increments from the first part of the time-steps and the explicit updates, which are

$$R_\psi = \underbrace{\frac{\rho^{(n)}\psi^{(n)}}{\Delta t}}_{\text{previous time}} \underbrace{- \nabla\cdot\left((1-\alpha)\left[\phi^{(n)}\psi^{(n)}_{\text{HO}} - \rho_f K \nabla_S \psi^{(n)}\right]\right) + (1-\alpha)S^{(n)}_\psi}_{\text{increments from first part of timestep}} \tag{23}$$

$$\underbrace{- \nabla\cdot\left(\alpha(1-\beta)\phi^{k-1}\psi^{k-1}_{\text{HO}}\right) - \nabla\cdot\left(\alpha\beta\gamma\phi^{k-1}\psi^{k-1}_{\text{HOC}}\right) + \nabla\cdot\left(\alpha\rho_f K \nabla_{\text{noc}}\psi^{k-1}\right)}_{\text{explicit updates from previous iteration}}, \tag{24}$$

$$T_\psi = \alpha S^{k-1}_\psi.$$

The reason for writing the matrix in this (OpenFOAM) form is so that one Jacobi iteration (labeled by j) can be expressed as

$$\psi^j = A_\psi^{-1}\left(H_\psi \psi^{j-1} + R_\psi + T_\psi\right), \tag{25}$$

which will be used in Section 2.4. The RHS term T_ψ is written separately from R_ψ because in Equation C4, $T_{\mathbf{u}}$ includes the pressure gradient term of the momentum equation when formulating the pressure equation.

As in WWKS23, "the resulting linear equation system is solved with the standard OpenFOAM bi-conjugate gradient solver with a diagonal incomplete LU preconditioner (DILU)." A significant difference to WWKS23 is that no more than one solver iteration is employed per outer iteration. The proof in WWKS23 that the first-order scheme is monotonic assumes that the linear system is solved exactly which is not the case here. However, we will see in Section 3.1.2 that monotonicity is maintained for large Courant numbers with just one solver iteration. This is straightforward to prove for Jacobi iterations, but we are not aware of a proof for the DILU solver that we are using.

2.2.4. Applying Flux-Corrected Transport (FCT)

FCT is applied to achieve monotonicity for the monotonic advection test case (Section 3.1.2). It is not used in the solution of the Navier-Stokes equations (Sections 3.2 and 3.3), simply because of incompatibilities between the Navier-Stokes code and the FCT implementation. This is a situation that needs to be rectified.

Section 2.3 describes the flux limiter γ, which is set based on Courant number, to ensure that solutions with large Courant numbers are smooth. In Section 3.1.2 where FCT is used, γ is set to one, so FCT is a different form of flux limiting to γ.

The first note of caution in applying FCT to implicit advection is that we should not expect $\psi_C^{(n+1)}$ to be bounded by $\psi_C^{(n)}$ and face neighbors $\psi_N^{(n)}$, because, with Courant numbers larger than one, extrema should be able to move beyond neighboring cells in one time-step (as discussed by WWKS23). The FCT algorithm of Zalesak (1979) uses $\psi_C^{(n)}$ and $\psi_N^{(n)}$ to bound $\psi_C^{(n+1)}$ as well as using the first-order solution at $n + 1$. When using implicit time-stepping, we can only use the first-order solution at $n + 1$ at cell C and neighbors, N, to bound the high-order solution. As a result, this means that applying FCT to an implicit scheme will be more diffusive than applying it to an explicit scheme.

The next issue in applying FCT is the requirement of the availability of a first-order, monotonic solution. This was available in the implicit version of MPDATA in WWKS23 since MPDATA is expressed as a correction on the first-order upwind scheme. However, when using RK-IMEX time-stepping, the first equation solved is Equation 16 which gives the high-order solution. The high-order correction is calculated explicitly, but the low-order part is solved with the high-order correction as part of the right hand side. This dramatically improves accuracy in

comparison to first solving a first-order solution and then applying a high-order correction. This means that, to get the necessary monotonic solution to use to correct the high-order solution, Equation 18 must be solved separately with $\gamma = 0$ and $k = 1$ to give the monotonic solution, ψ^d. Therefore, the monotonic solution, ψ^d, is the solution of Equation 18 but with

$$R_\psi = \frac{\rho^{(n)}\psi^{(n)}}{\Delta t} - \nabla\cdot\left((1-\alpha)\left[\phi^{(n)}\psi_{1\text{st}}^{(n)} - \rho_f K\nabla_2\psi^{(n)}\right]\right) + (1-\alpha)S_\psi^{(n)} - \nabla\cdot\left(\alpha(1-\beta)\phi^{k-1}\psi_{1\text{st}}^{k-1}\right), \tag{26}$$

and with A_ψ and H_ψ the same as for the full solution. Once ψ^d, ψ^k and the corresponding fluxes are available, then the FCT algorithm can be applied as described in WWKS23.

2.3. Numerical Analysis and Stability Parameters

Stability analysis is used to set the parameters α, β and γ while optimizing accuracy and cost.

1. The temporal off-centering $\alpha \in \left[\frac{1}{2}, 1\right)$ needs to be $\frac{1}{2}$ for second-order accuracy in time but can be larger for improved stability at the expense of temporal accuracy.
2. The implicit/explicit flag β is zero where the advection is calculated explicitly and one where it is implicit.
3. The flux limiter $\gamma \in (0, 1]$ limits the high-order spatial correction.

It is essential that α, β and γ are defined on faces rather than cell centers, and that they are inside the divergence in Equation 16, otherwise local conservation is violated. However, for the linear numerical analysis, these parameters are assumed uniform.

The stability of the advection depends on the Courant number, which can be defined for the finite volume cell of an arbitrary mesh as

$$c = \frac{1}{2}\frac{\Delta t}{\mathcal{V}}\sum_f |U_f|, \tag{27}$$

where $U_f = \mathbf{u}\cdot\mathbf{S}_f$ is the volume fluxes through each face. In order to set parameters α, β and γ on faces, the Courant number on the face is calculated as the maximum of the Courant numbers either side of the face

$$c_f = \max(c_N, c_C). \tag{28}$$

For stably stratified flow, stability also depends on the Brunt–Väisälä frequency defined as

$$N = \sqrt{\max\left(-\frac{\mathbf{g}\cdot\nabla\overline{\theta}}{\overline{\theta}},\ 0\right)}, \tag{29}$$

where $\mathbf{g} = (0, 0, -g)$ is the acceleration due to gravity and $\overline{\theta}$ is the reference profile potential temperature (see Section 2.4).

We analyse the simplified, one-dimensional system with advection and the vertical component of gravity waves

$$\frac{\partial\Psi}{\partial t} + U_0\frac{\partial\Psi}{\partial x} = iN\Psi, \tag{30}$$

where $\Psi = b + iNw$, $i = \sqrt{-1}$, buoyancy $b = g\theta'/\overline{\theta}$ and U_0 is the uniform, constant horizontal velocity. Equation 30 is a simplification of the compressible Boussinesq w and b equations of Durran and Blossey (2012) that ignores horizontal pressure gradients. We consider a uniform grid with spacing Δx, indexed by j and $c = \Delta t U_0/\Delta x$. The implicit-explicit, 2nd-order Runge-Kutta time-stepping with cubic-upwind advection is

$$
\begin{aligned}
1^{\text{st}}\text{ iteration}: \ \Psi_j^1 = \ & \Psi_j^{(n)} - (1-\alpha\beta)\, c\left(\Psi_j^{(n)} - \Psi_{j-1}^{(n)}\right) - \alpha c\beta\left(\Psi_j^1 - \Psi_{j-1}^1\right) \\
& - \gamma c\left(\Psi_{HOCj+1/2}^{(n)} - \Psi_{HOCj-1/2}^{(n)}\right) \\
& - iN\Delta t(1-\alpha)\Psi_j^{(n)} - iN\Delta t\alpha\Psi_j^1,
\end{aligned} \tag{31}
$$

$$
\text{Cubic correction}: \ \Psi_{HOCj+1/2} = \frac{2\Psi_{j+1} - \Psi_j - \Psi_{j-1}}{6}, \tag{32}
$$

$$
\begin{aligned}
2^{\text{nd}}\text{ iteration}: \ \Psi_j^{(n+1)} = \ & \Psi_j^{(n)} - (1-\alpha)\, c\left(\Psi_j^{(n)} - \Psi_{j-1}^{(n)}\right) - \alpha c(1-\beta)\left(\Psi_j^1 - \Psi_{j-1}^1\right) \\
& - \alpha c\beta\left(\Psi_j^{(n+1)} - \Psi_{j-1}^{(n+1)}\right) \\
& - \gamma(1-\alpha)\, c\left(\Psi_{HOCj+1/2}^{(n)} - \Psi_{HOCj-1/2}^{(n)}\right) \\
& - \gamma\alpha c\left(\Psi_{HOCj+1/2}^1 - \Psi_{HOCj-1/2}^1\right) \\
& - iN\Delta t(1-\alpha)\Psi_j^{(n)} - iN\Delta t\alpha\Psi_j^{(n+1)}.
\end{aligned} \tag{33}
$$

We consider waves with wavenumber k in order to perform von-Neumann stability analysis, so that each wave takes the form

$$
\Psi_j^{(n)} = \mathcal{A}^n e^{ijk\Delta x}, \tag{34}
$$

where $\mathcal{A}$ is the amplification factor. Note that k is used to count outer iterations in other sections but is used as wavenumber in this section. Substituting Equation 34 into Equations 31–33 gives a complicated equation for $\mathcal{A}$ as a function of α, β, γ, c, $N\Delta t$ and $k\Delta x$

$$
\mathcal{A} = \frac{1 - c\left(1 - e^{-ijk\Delta x}\right)\left(1 - \alpha + \alpha(1-\beta)\,\mathcal{A}^1\right) - \gamma c\mathcal{A}^h\left(1 - \alpha + \alpha\mathcal{A}^1\right) - iN\Delta t(1-\alpha)}{1 + \alpha c\beta(1 - e^{-ijk\Delta x}) + iN\Delta t\alpha}, \tag{35}
$$

where

$$
\begin{aligned}
\mathcal{A}^h &= \frac{1}{6}\left(2e^{ijk\Delta x} - 3 + e^{-2ijk\Delta x}\right), \\
\mathcal{A}^1 &= \frac{1 - (1-\alpha\beta)\, c\left(1 - e^{-ijk\Delta x}\right) - \gamma c\mathcal{A}^h - iN\Delta t(1-\alpha)}{1 + \alpha c\beta(1 - e^{-ijk\Delta x}) + \alpha iN\Delta t}.
\end{aligned}
$$

For stability we require $|\mathcal{A}| \le 1 \ \ \forall \ \ k\Delta x \in [0, 2\pi]$. Therefore ranges of values of α, β, γ, c and $N\Delta t$ are considered and the maximum $|\mathcal{A}|$ is found over 80 equally spaced values of $k\Delta t$. We already have from WWKS23 and from Section 2.2.2 that for $\gamma = 0$ (no high-order in space) we need $\alpha < 1 - 1/c$ for monotonicity. In order to find when implicit advection is needed ($\beta = 1$) in combination with cubic upwind advection ($\gamma = 1$) without interaction with gravity wave ($N\Delta t = 0$), $\max_{k\Delta x \in [0,2\pi]}(|\mathcal{A}|)$ is plotted as a function of c for $\beta = 0/1$ and $\gamma = 0/1$ in the top left panel of Figure 2 for, $\alpha = \frac{1}{2}$ and for

$$
\alpha = \max\left(\frac{1}{2},\ 1 - \frac{1}{c}\right). \tag{36}
$$

The explicit scheme ($\beta = 0$) with $\alpha = \frac{1}{2}$, is stable up to $c = 1$ for the first-order scheme ($\gamma = 0$) and up to $c = 0.88$ for cubic upwind ($\gamma = 1$). Introducing implicit advection ($\beta = 1$) stabilizes first-order advection for all $\alpha \ge \frac{1}{2}$. However cubic upwind ($\gamma = 1$), with $\beta = 1$ (implicit) and with $\alpha = \frac{1}{2}$ (second-order in space) is only stable for $c \le 2$. This is the motivation for Equation 36 to calculate α, which stabilizes the implicit cubic upwind for all Courant numbers.

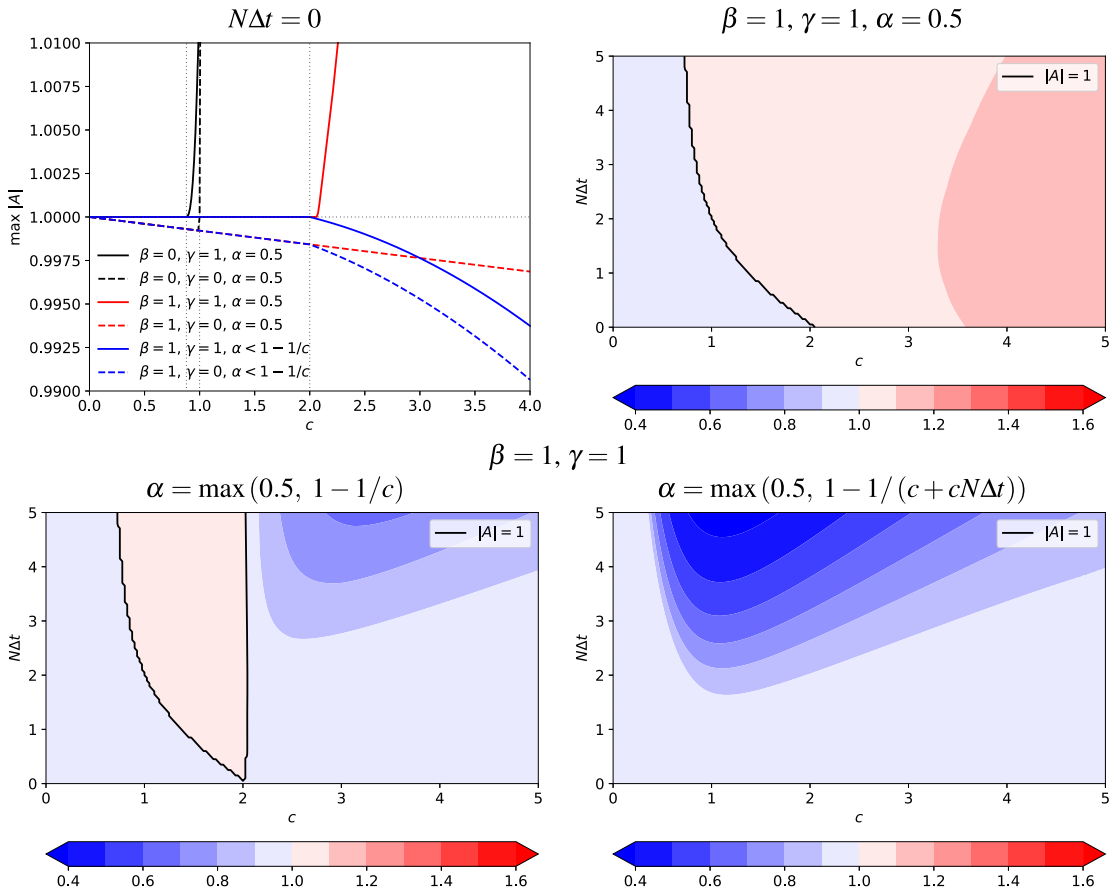

Figure 2. Numerical analysis of implicit/explicit cubic upwind solution of Equation 30. In each panel, the maximum of the magnitude of amplification factor $|\mathcal{A}|$ over all wavenumbers, $k\Delta x \in [0, 2\pi]$ is plotted ($\max_{k\Delta x}|\mathcal{A}|$). Top left: $\max_{k\Delta x}|\mathcal{A}|$ as a function of c for $N\Delta t = 0$ for schemes with various combinations of α, β and γ. The other panels show $\max_{k\Delta x}|\mathcal{A}|$ contoured as a function of c and $N\Delta t$ with $|\mathcal{A}| = 1$ contoured black, again for different combinations of α, β and γ. The formulation for α in the bottom right is unconditionally stable so there is no contour for $|\mathcal{A}| = 1$.

The maximum of $|\mathcal{A}|$ over all $k\Delta x \in [0, 2\pi]$ for a range of Courant numbers and a range of $N\Delta t$ is contoured in Figure 2 all using $\beta = 1$ (implicit advection) and $\gamma = 1$ (cubic upwind advection). The top right showing $|\mathcal{A}|$ for $\alpha = \frac{1}{2}$ confirms the instability for $c > 2$ for $N\Delta t = 0$ and shows that this instability occurs for lower Courant numbers as $N\Delta t$ increases. If we use Equation 36 to calculate α (as worked for $N\Delta t = 0$) then the bottom left of Figure 2 shows that the scheme is now stable for $c > 2$, leaving an instability that occurs for lower Courant numbers as $N\Delta t$ grows. If instead we use

$$\alpha = \max\left(\frac{1}{2},\ 1 - \frac{1}{c + cN\Delta t}\right), \tag{37}$$

(bottom right of Figure 2) then we get stability for all c and $N\Delta t$ without introducing overly large values of α for small c for any value of $N\Delta t$.

Based on this analysis we should be able to use $\gamma = 1$ for all c. However, we found that $\gamma = 1$ can lead to spurious but stable oscillations when solving the fully compressible Navier-Stokes equations with large Courant numbers, likely caused by incorrect interactions between advection and other waves (Section 3.3). Therefore, the value of γ is reduced for $c > 2$. The final values of α, β and γ that are used in the solution of the Navier-Stokes equations are given in Table 1. It is possible that a better solution would be to use FCT, but this has not yet been explored for solving the Navier-Stokes equations adaptive implicitly.

Table 1
Values of α (Temporal Off-Centering), β (Implicit Switch) and γ (High-Order Flux Limiter) That Are Used in the Numerical Solution of the Navier-Stokes Equations

α:	$\max\left(\frac{1}{2},\ 1-\frac{1}{c+cN\Delta t}\right)$
β:	$\begin{cases}0 & c<0.8\\ 1 & c\geq 0.8\end{cases}$
γ:	$\begin{cases}1 & c<2\\ \frac{4-c}{2} & c\in[2,4]\\ 0 & c>4.\end{cases}$

2.4. Solution of the Fully Compressible Navier-Stokes Equations

The Navier-Stokes equations are formulated as

$$\frac{\partial \rho}{\partial t}+\nabla\cdot\rho\mathbf{u}=0, \tag{38}$$

$$\frac{\partial \rho\theta'}{\partial t}+\nabla\cdot\rho\mathbf{u}\theta'-\nabla\cdot\left(\rho\kappa\nabla\theta'\right)=-\rho w\frac{d\overline{\theta}}{dz}, \tag{39}$$

$$\frac{\partial \rho\mathbf{u}}{\partial t}+\nabla\cdot\rho\mathbf{u}\mathbf{u}-\nabla\cdot(\rho\nu\nabla\mathbf{u})=-\rho\left(\frac{\theta'}{\overline{\theta}}\mathbf{g}+c_p\theta\nabla\pi'\right), \tag{40}$$

with the density ρ, potential temperature $\theta = T/\pi$, the velocity vector $\mathbf{u}$, and the Exner pressure defined as $\pi = \left(p/p_r\right)^{R/c_p}$, where R is the gas constant of dry air, c_p the specific heat of dry air at constant pressure p and $p_r = 10^5$ Pa is a constant references pressure. Furthermore, κ is the thermal diffusivity and ν is the kinematic viscosity. The primed thermodynamic variables $\theta' = \theta - \overline{\theta}$ and $\pi' = \pi - \overline{\pi}$ represent perturbations with respect to reference profiles $\overline{\theta}(z)$ and $\overline{\pi}(z)$ in hydrostatic balance given as

$$c_p\overline{\theta}\frac{d\overline{\pi}}{dz}=\mathbf{g}\cdot\mathbf{k}=-g. \tag{41}$$

The temperature and pressure satisfy the ideal gas law which is written in terms of perturbation quantities

$$\pi'=\left(\frac{\rho R\left(\overline{\theta}+\theta'\right)}{p_r}\right)^{\frac{R}{c_v}}-\overline{\pi}, \tag{42}$$

where $c_v = c_p - R$ is the specific heat capacity at constant volume. The formulation in the perturbation variables is beneficial for the design of the numerical integration, its initialization and regularization.

The advection terms of the momentum and potential temperature equations are treated implicitly (where needed) while terms involving acoustic and gravity wave propagation are held fixed, and then the advection terms are held fixed while acoustic and gravity waves are treated implicitly for the solution of the Helmholtz (pressure) equation. Outer iterations are necessary for convergence.

Details of the solution of the Navier-Stokes equations are provided in Appendix C.

3. Results of Test Cases

Results are presented of deformational flow advection on the surface of a sphere Section 3.1, buoyant flow in two and three dimensions Section 3.2 and stably stratified flow in two dimensions Section 3.3.

3.1. Deformational Flow Advection on the Sphere

WWKS23 presented results of deformational flow advection on a unit sphere (Lauritzen et al., 2012) using the adaptively implicit MPDATA on full latitude-longitude grids, skipped latitude-longitude grids, hexagonal-icosahedra and cubed-sphere meshes. The same grids are studied here (Table 2) but we use the method-of-lines advection scheme with a quasi-cubic spatial correction. These linear advection tests all use $\gamma = 1$ rather than γ from Table 1. This gives the full high-order spatial correction for all Courant numbers and was predicted to be stable by the numerical analysis in Section 2.3. Some linear advection tests are repeated with $\gamma < 1$ for $c > 2$, as defined as in Table 1, to assess the impact on solution accuracy. The stability of using $\gamma = 1$ for all Courant numbers is in contrast to the results of WWKS23 who needed to reduce the high-order spatial correction for stability with large Courant numbers. The other important difference from WWKS23 is that only one solver iteration is used per outer iteration (with two outer iterations per time-step). All of the cases from WWKS23 were repeated but only select results are presented.

Table 2
Resolutions and Time-Steps for Deformational Flow Advection With Δx a Typical Cell Center to Cell Center Distance in Degrees Latitude

Mesh type	Nominal	N. cells	Δx	Δt
Latitude-longitude	120 × 60	7,080	3.0°	0.01
	240 × 120	28,800	1.5°	0.005
	480 × 240	114,720	0.75°	0.0025
Skipped latitude-longitude	120 × 60	5,310	3.0°	0.01
	240 × 120	21,750	1.5°	0.005
	480 × 240	88,470	0.75°	0.0025
Cubed-sphere (Cn is $n \times n \times 6$)	C30	5,400	3.2°	0.01
	C60	21,600	1.6°	0.005
	C120	86,400	0.8°	0.0025
Hexagonal-icosahedral	HR6	10,242	2.4°	0.01
	HR7	40,962	1.2°	0.005
	HR8	163,842	0.6°	0.0025
	HR9	655,362	0.3°	0.00125

Note. The dimensionless time-step is the one that gives a nominal (global average) Courant number of one. A complete revolution takes 5 time units.

3.1.1. Smooth Gaussian Hill Shaped Tracer

Figure 3 shows the concentration at half of the end time (2.5 time units) for the deformational flow advection of two Gaussian hill shaped tracer distributions (Lauritzen et al., 2012). We consider the flow over the poles of a rotated latitude-longitude grid and flow through a hexagonal icosahedral mesh using $\gamma = 1$. Pink/purple line contours show Courant numbers which are large over the latitude-longitude poles. This test is designed to test order of accuracy rather than boundedness so it is run without FCT and indeed undershoots are created. The advection passes through the poles of the grid without creating noticeable artifacts. The results are visually identical for the latitude-longitude mesh using γ from Table 1. This is likely because the resolution is high where the Courant number is high, so the local use of first-order spatial discretization does not reduce accuracy.

The ℓ_2 error norms at the end time (5 time units) are calculated for the simulations listed in Table 2 and are plotted as a function of Δx in Figure 4. These simulations use $\gamma = 1$ (cubic in space) apart from two simulation on the latitude-longitude grid which use $\gamma < 1$ for $c > 2$ (Table 1). This reduction in accuracy where the resolution is high increases the error by about 0.2%. The convergence on the hexagonal grid is less than second-order. This is because the cubic correction is not well suited to the hexagonal grid. Second-order accurate results can be achieved on the hexagonal grid by using a quadratic reconstruction of face values (not shown) rather than the cubic scheme which is designed to give third-order accuracy at regular cell centers, rather than at faces. However, the development of an accurate spatial discretization on the hexagonal grid is peripheral to the main focus of this paper, which is focused on the novel adaptively implicit time-stepping. The use of a variety of grids highlights the generality of the approach.

When the time-step is increased while keeping spatial resolution fixed on the cubed sphere grid (right panel of Figure 4), the error remains low up to a Courant number of two, and then increases proportional to the time-step while remaining stable, as expected and required.

3.1.2. Slotted Cylinder

In order to test monotonicity of the first-order solution and to test the application of FCT, a tracer field in the shape of two slotted cylinders are advected in deformational flow (Lauritzen et al., 2012) on a rotated latitude-longitude grid and a hexagonal icosahedra (Figure 5). An initial monotonic first-order solution is an essential part of FCT. A monotonic solution is guaranteed by the first-order implicit in time and first-order upwind in space discretization (e.g., WWKS23). Figure 5 shows that solutions are bounded at the final time after application of FCT, implying that the first-order solutions are also bounded, as required.

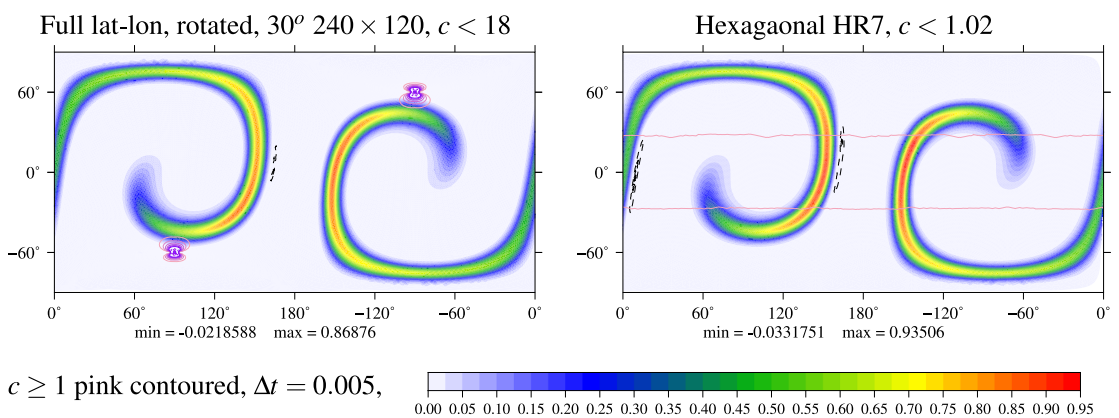

Figure 3. Deformational flow on the sphere advecting Gaussian hill shaped distributions of ψ at the half-time 2.5 using $\gamma = 1$. Dashed contours at $\psi = -10^{-2}, -2 \times 10^{-2}, -3 \times 10^{-2}$.

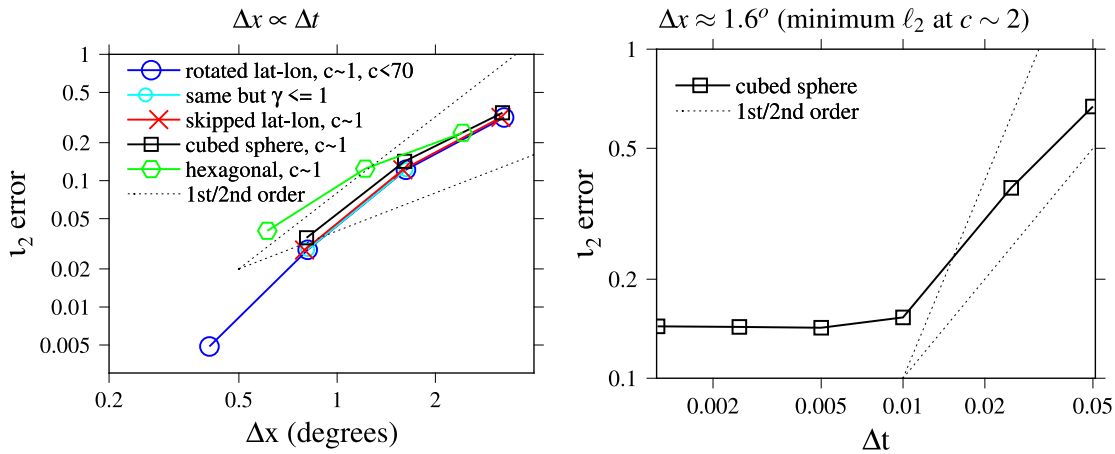

Figure 4. Error norms for deformational flow advection of Gaussian hill shaped distributions. The left panel shows errors as a function of spatial resolution while keeping the time-step proportional. The right panel shows errors as a function of time-step on the C60 cubed sphere. Unless otherwise stated, $\gamma = 1$.

The maximum tracer concentration as a function of time and the normalized change in total tracer mass are shown in Figure 6. The minimum tracer concentration is not shown as it is always 0.1 (the initial minimum). The maximum concentration never exceeds the initial maximum, as required. The changes in mass are of the order 10^{-14} which is, importantly, machine precision rather than the higher value of solver convergence.

3.2. Buoyancy Driven Flow

Positive buoyancy combined with latent heat of condensation can create strong updrafts which, in the presence of high vertical resolution and moderate time-steps, can lead to large vertical Courant numbers. Tests are presented of two spatially resolved, two-dimensional dry buoyant flows; a rising bubble (Bryan & Fritsch, 2002) and Rayleigh-Bénard convection (Shipley et al., 2022). In order to resolve the details of convective flows such as these, isotropic resolution is used. This gives Courant numbers greater than one in the horizontal and vertical when combined with moderate time-steps. These tests are used to compare fully explicit, fully implicit and adaptive implicit time-stepping for advection, combined with implicit treatment of acoustic and gravity waves. The simulations use α and γ as defined in Table 1. The fully explicit simulations use $\beta = 0$, the implicit solutions use $\beta = 1$ and the adaptive implicit (IMEX) solutions use β from Table 1.

3.2.1. Rising Bubble

The dry rising bubble test of Bryan and Fritsch (2002) uses an $x - z$ domain $[-10\,\text{km}, 10\,\text{km}] \times [0, 10\,\text{km}]$ surrounded by zero flux boundary conditions discretized using a $\Delta x = \Delta z = 100\,\text{m}$ and subject gravity $g = 9.81\,\text{ms}^{-2}$. The simulation is inviscid and initially stationary with potential temperature defined as

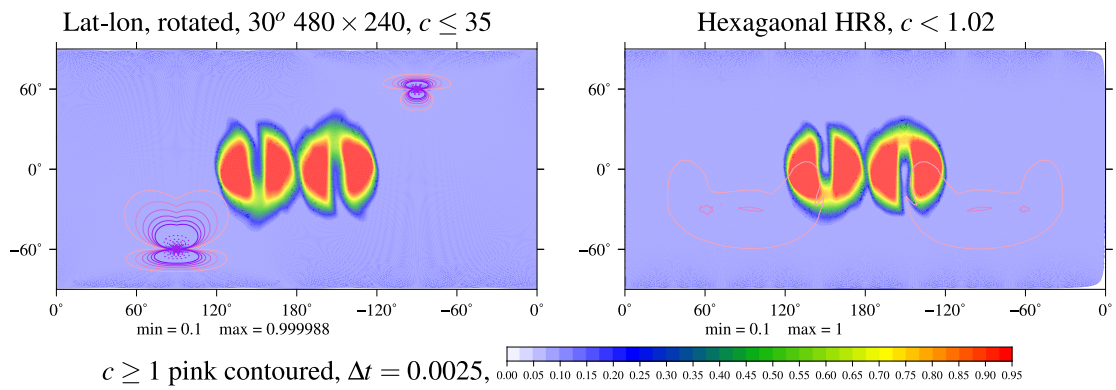

Figure 5. Final results of deformational flow advection of slotted cylinders on the sphere.

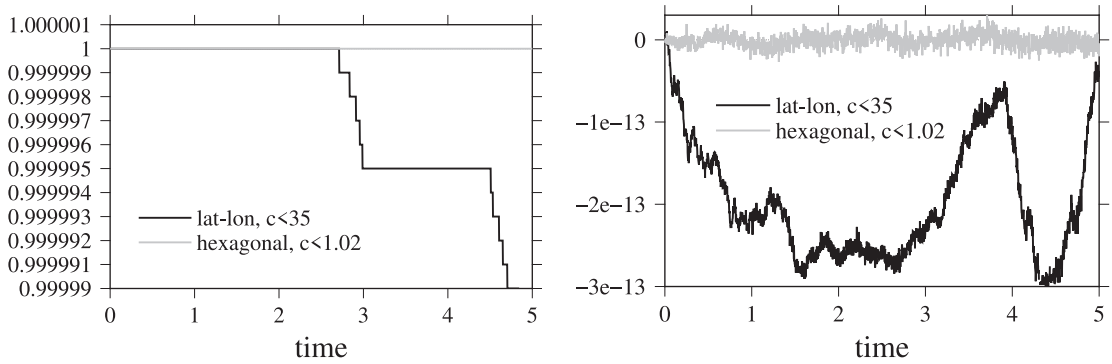

Figure 6. Maximum concentration and normalized mass change during deformational flow advection of slotted cylinders on the sphere. The minimum is not plotted because it does not change from 0.1. The normalized tracer mass change is the change in mass divided by the initial tracer mass.

$$\theta = \begin{cases} \left[300 + 2\cos^2\left(\frac{\pi r}{2}\right)\right] \text{K} & r \le 1 \\ 300 \text{ K} & \text{otherwise,} \end{cases} \tag{43}$$

$$\text{where } r^2 = \frac{(x - x_c)^2}{A_x^2} + \frac{(z - z_c)^2}{A_z^2}, \tag{44}$$

$$(x_c, z_c) = (0, 4.5 \text{ km}),\ A_x = A_z = 2 \text{ km}. \tag{45}$$

The initial Exner pressure perturbation is zero. The potential temperature anomalies from 300 K are shown in Figure 7 after 1,000 s using time-steps from 2 to 20 s. For $\Delta t = 2$ s, the Courant number remains below 0.35 and for $\Delta t = 5$ s, below 0.88. This means that the adaptively implicit (IMEX) results are identical to the explicit results. The results using implicit advection with small time-steps have small differences from the explicit solutions that are difficult to see in Figure 7. Using $\Delta t = 10$ s and $\Delta t = 20$ s the maximum Courant numbers are 1.76 and 3.38 so the simulations using explicit advection are unstable. At $\Delta t = 10$ s, the boundary between implicit and explicit time-stepping in the IMEX simulation has initiated a disturbance in the bubble leading edge which is unrealistic but has not lead to model instability. At $\Delta t = 20$ s, implicit and IMEX both have dispersion errors seen as ripples behind the leading bubble edge, consistent with the reduced accuracy associated with the large time-step. Therefore the adaptively implicit time-stepping is behaving as required: enabling large stable Courant numbers locally but without ensuring accuracy where the Courant number is large. The test case would likely benefit from the use of FCT for advecting θ' to avoid undershoots and ripples in θ'.

The simulations using implicit time-stepping for advection are limited to use one solver iteration for the advection, which ensures that the cost of the advection does not scale with the time-step. However the larger the time-step, the more iterations are needed in the pressure solver (to solve the Helmholtz equation for Exner pressure). Figure 8 shows the maximum Courant number as a function of time for each simulation and the number of iterations of the pressure solver per 20 s of simulated time (stopping criteria defined in Section C4). The bubble accelerates throughout the simulations but the number of iterations per time-step remains more uniform. Importantly, using a larger time-step always results in fewer iterations in the pressure solver per 20 s of simulated time. For comparable time-steps, explicit and IMEX simulations use fewer iterations than globally implicit time-stepping for advection.

Estimates for CPU runtimes are shown in the legends in Figure 8. The first important remark about the CPU time is that it scales close to linearly with time-step—doubling the time-step approximately halves the run time, even when comparing implicit and explicit simulations. The code is identical for the implicit, explicit and IMEX simulations, but the Courant number threshold for the calculation of β is different; for the explicit simulations, β is calculated to be uniformly zero, for the implicit simulations, β is uniformly one and for the IMEX simulations,

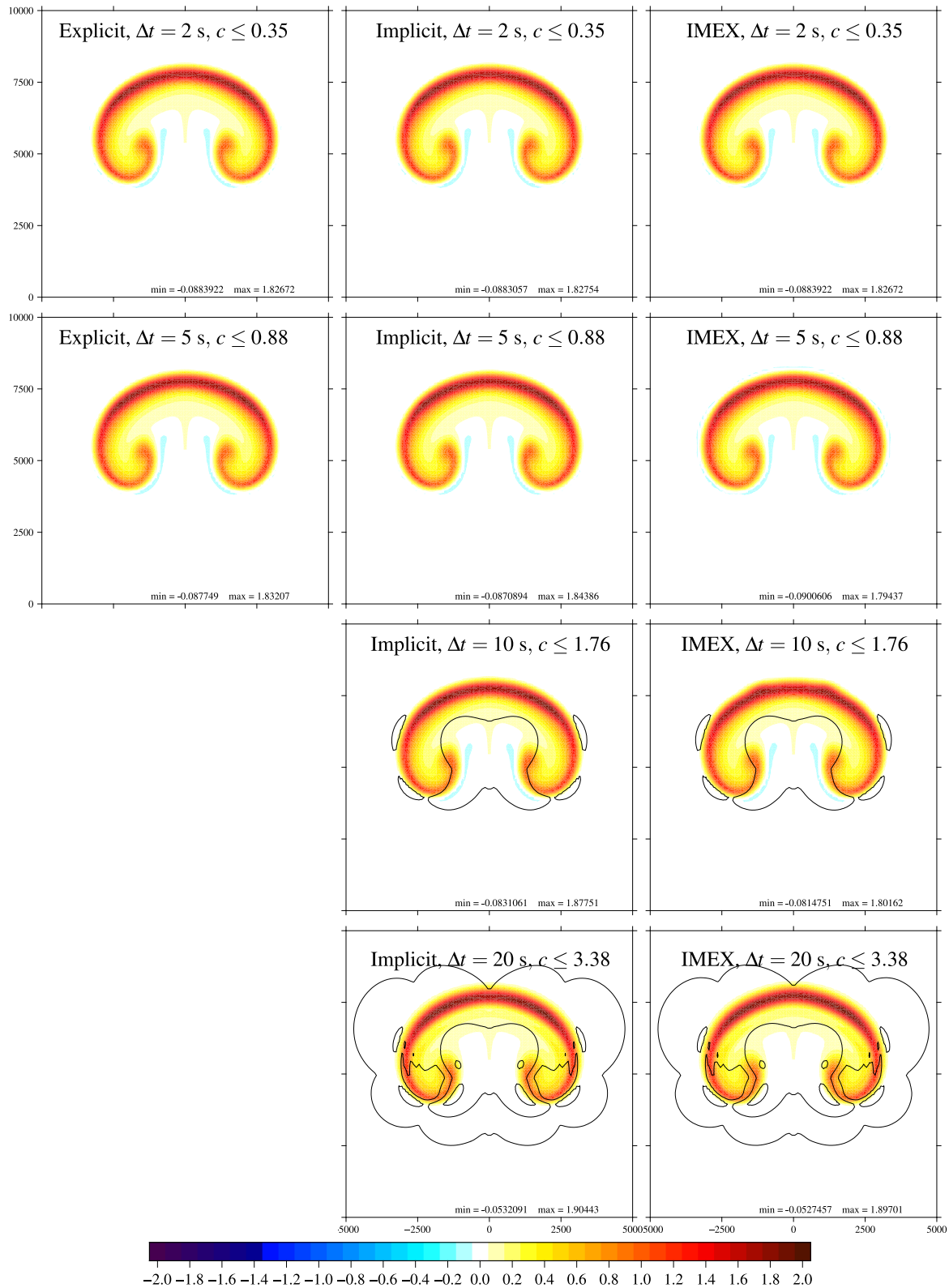

Figure 7. Potential temperature anomalies (shaded, K) of the rising bubble simulation after 1,000 s of simulation time using either explicit, implicit or IMEX advection with different time-step sizes Δt, and different maximum Courant numbers c. Courant numbers above 1.0 are line contoured in steps of 1.0.

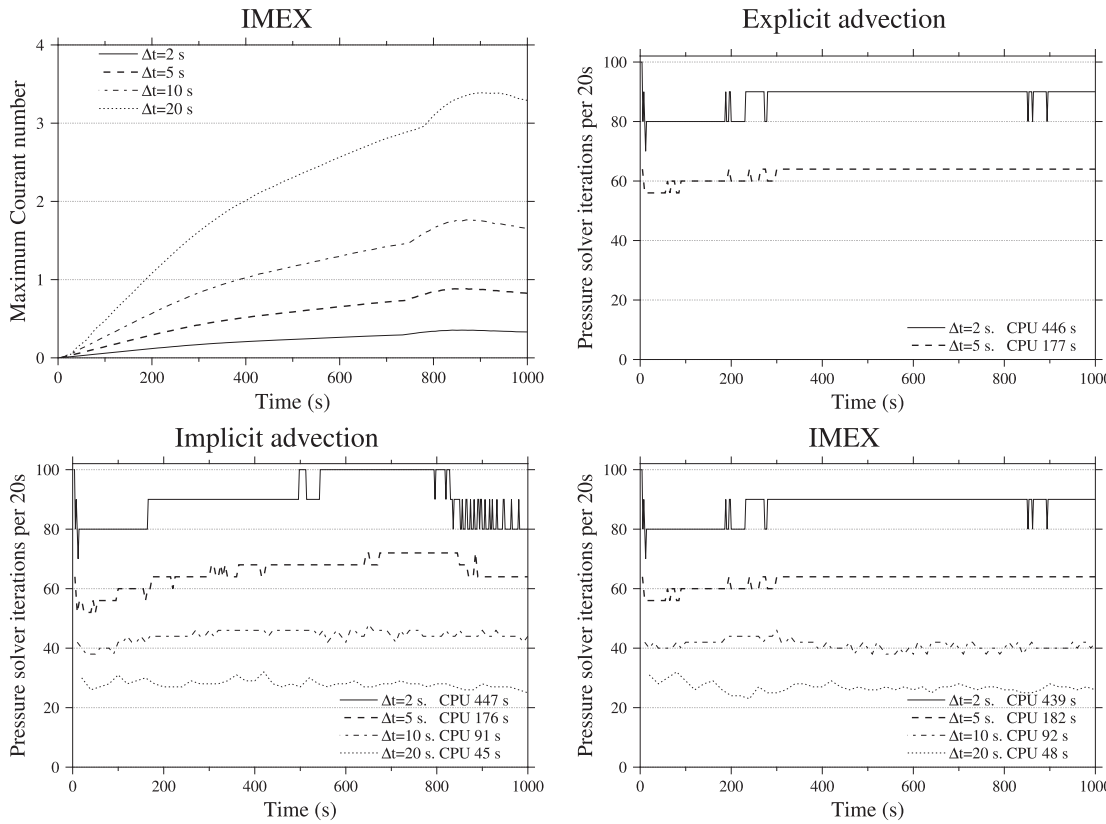

Figure 8. Maximum Courant number of IMEX simulations and total number of pressure solver iterations per 20 s of simulated time for the solutions of the rising bubble using explicit, implicit and IMEX advection. Increasing the time-step always leads to fewer pressure solver iterations per second of simulated time. Total CPU times for each simulation are shown in the legends.

β is one where the Courant number is above 0.8. This means that the IMEX simulations should be identical to the explicit simulations for $\Delta t = 2$ s, which is indeed the case. At $\Delta t = 5$ s, all three simulations have similar run times, showing that the implicit advection does not significantly add to the CPU time. At $\Delta t = 10$ s and $\Delta t = 20$ s, the explicit solution is not stable and the IMEX and implicit solutions are much faster. The implicit advection iteration is having negligible influence on the total cost. However, if one were writing a purely explicit scheme, further gains could be made because no checks would be made on the Courant number and no matrix preconditioners would be executed for the advection.

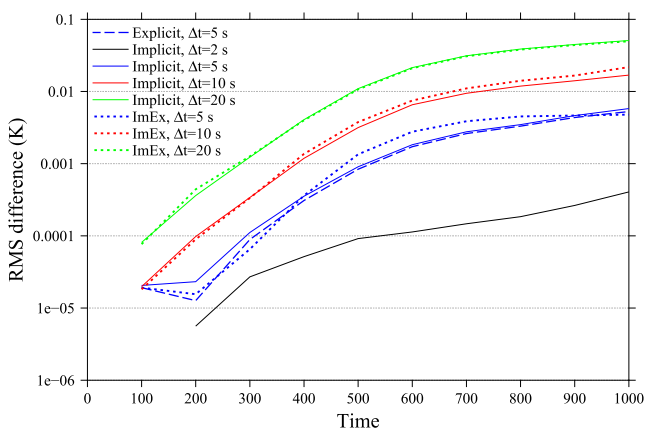

Figure 9. Root mean square differences between the temperature anomalies of each simulation of the rising bubble and the explicit solution with $\Delta t = 2$ s. Implicit or IMEX advection gives similar results to explicit for the same time-step but the larger the time-step the greater the difference.

In Figure 9, the root mean square average difference between the $\Delta t = 2$ s explicit simulation and the other simulations are shown as a function of time. The $\Delta t = 2$ s IMEX simulation results are identical to the $\Delta t = 2$ s explicit results so the zero differences are not shown on the log-scale. The $\Delta t = 2$ s implicit time-step results are closest to the $\Delta t = 2$ s explicit results. The $\Delta t = 5$ s results have the next smallest RMS differences, again with the explicit and IMEX results being identical. As the time-steps increase the RMS differences increase and the implicit and IMEX results remain close. The adaptively implicit advection is behaving as required—accuracy is reduced but large time-steps are possible.

3.2.2. Rayleigh-Bénard Convection

Rayleigh-Bénard convection occurs between a warm flat plate, a distance L_z below a cool flat plate with temperature difference $\Delta\theta$. It is governed by two dimensionless numbers; the Rayleigh number (the ratio of buoyancy forcing

Table 3
Parameters for Simulating Rayleigh-Bénard Convection With Prandtl Number One

Parameter				Units
Rayleigh number	Ra	10^6	10^8	–
Gravitational acceleration	g	10	10	m s^{-2}
Domain height	L_z	1	1	m
Domain width	L_x, L_y	2.02	2.02	m
Top to bottom temperature difference	ΔT	1	1	K
Average temperature	$\overline{T}$	1000	1000	K
Kinematic viscosity	ν	10^{-4}	10^{-5}	m s^{-2}
Gas constant	R	100	100	J kg^{-1} K^{-1}
Total simulation time		1000	1000	s
Time-step	Δt		0.2	s
Grid spacing	Δx, Δz		0.01	m

Note. Grid spacing, time-steps and maximum Courant numbers for the Ra $= 10^6$ simulations are in Table 4.

to viscous diffusion) and the Prandtl number (the ratio of the diffusion of momentum to the diffusion of buoyancy)

$$\mathrm{Ra} = \frac{\rho \Delta\theta\, L_z^3 g}{\overline{\theta}\nu\kappa}, \tag{46}$$

$$\mathrm{Pr} = \frac{\nu}{\kappa}. \tag{47}$$

In the atmosphere Pr $= 0.7$ and in the convective boundary layer, the Rayleigh number could be 10^{16} (Shipley et al., 2022). In this parameter regime, convection occurs in narrow plumes, making this a suitable test of implicit advection because Courant numbers are only large in a small fraction of the domain. Computational constraints mean that we simulate Rayleigh-Bénard convection at much smaller Rayleigh numbers in two spatial dimensions, and one simulation in three dimensions, keeping the Rayleigh number large enough so that convection occurs in narrow plumes.

Rayleigh-Bénard convection is chaotic, so details of the time-stepping will influence any snapshot of the solution, but we do not want these details to significantly influence the solution statistics. We use the Nusselt number (the non-dimensionalized heat transfer)

$$\mathrm{Nu} = \frac{L_z}{\kappa\overline{\rho}\Delta\theta}\left\langle \rho w\theta' - \kappa\rho\frac{\partial\theta'}{\partial z}\right\rangle_V, \tag{48}$$

where $\langle\cdot\rangle_V$ is a volume average and $\overline{\rho}$ is the average density in the domain.

Simulations are presented for Rayleigh numbers of 10^6 and 10^8 spanning the range from laminar to turbulent convection and for a Prandtl number of one and with other parameters chosen to be in the nearly compressible regime with round numbers (Table 3). SI units are given in Table 3 but are not used for Rayleigh-Bénard convection throughout the rest of this section as they have no physical significance. The resolution, domain size and run length requirements are taken from Shipley et al. (2022). The spatial and temporal resolutions are in Tables 3 and 4.

Potential temperature perturbations at $t = 1000$ time units are shown in Figure 10 for two Ra $= 10^6$ simulations and the Ra $= 10^8$ simulation. The Ra $= 10^6$ simulations are laminar but not steady and the Ra $= 10^8$ simulation is chaotic with some turbulent eddies. The snapshot at Ra $= 10^8$ is similar to that of Shipley et al. (2022, their Figure 1b) but their simulation is at higher spatial and temporal resolution. Contours showing where the Courant number is greater than one are overlayed in Figure 10. There are no obvious artifacts where time-stepping switches from explicit to implicit and, for Ra $= 10^6$, the small time-step, explicit solution is similar to the larger time-step IMEX solution, despite the lower temporal accuracy where the Courant number reaches 4.1. A repeated IMEX simulation using $\Delta x = 0.02$, $\Delta t = 1$ but with $\gamma = 1$ for all c gives solutions that look identical to the middle plot of 10, with a root mean square difference of 12%, despite the potential for chaotic growth of differences.

Table 4
Maximum Courant Numbers for Simulations of Rayleigh-Bénard Convection With Ra $= 10^6$ at Different Resolutions in Two- and Three-Dimensions

Δt Δx, Δz	0.01	0.02	0.02 (3D)	0.04
0.05	0.51			
0.1		0.40		0.19
0.2		0.79		0.39
0.5		2.0		0.97
1		4.1	5.4	1.9
2.5		11.3		4.8
5				8.6

Results of a 3D simulation of Rayleigh-Bénard convection are shown in Figure 11. This uses the parameters for Ra $= 10^6$ with $\Delta x = \Delta y = 0.02$ and $\Delta t = 1$ giving a maximum Courant number of 4.7. The simulation in Figure 11 uses $\gamma < 1$ for $c > 2$. Isosurfaces of $\theta' = \pm 0.1$ are shown in the bottom of Figure 11. This demonstrates that exactly the same algorithms work in 3D, although the plumes are less vertically coherent.

Rayleigh-Bénard convection is chaotic so in order to assess the impact of adaptive implicit time-stepping and large time-steps, we compare the evolution of the Nusselt number between different simulations. The top panel of Figure 12 shows the domain average Nusselt number for Ra $= 10^6$ for three

$\mathrm{Ra} = 10^6$, explicit, $\Delta x = 0.02$, $\Delta t = 0.2$, $c < 0.8$

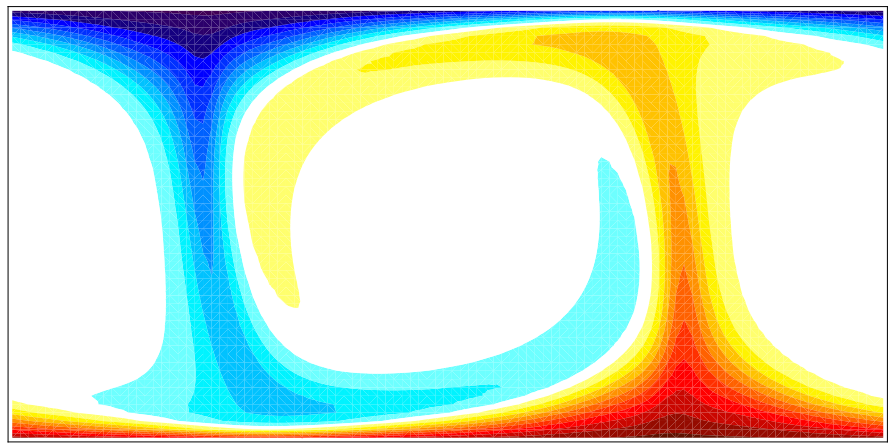

$\mathrm{Ra} = 10^6$, IMEX, $\Delta x = 0.02$, $\Delta t = 1$, $c < 4.1$

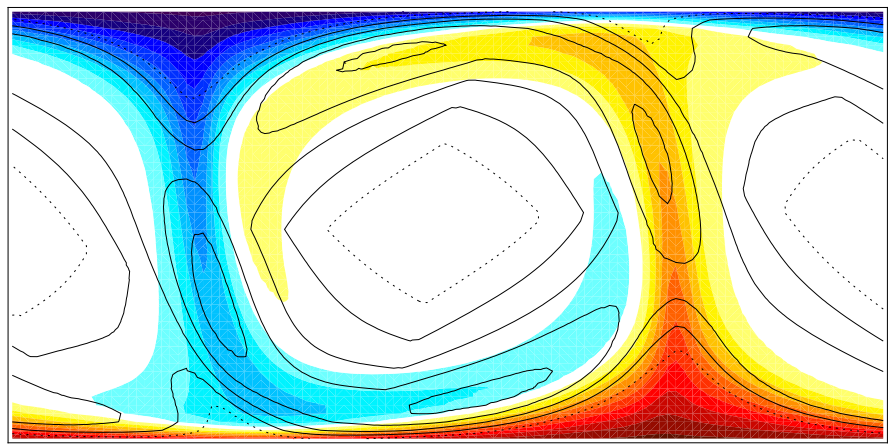

$\mathrm{Ra} = 10^8$, IMEX, $\Delta x = 0.01$, $\Delta t = 0.2$, $c < 2.0$

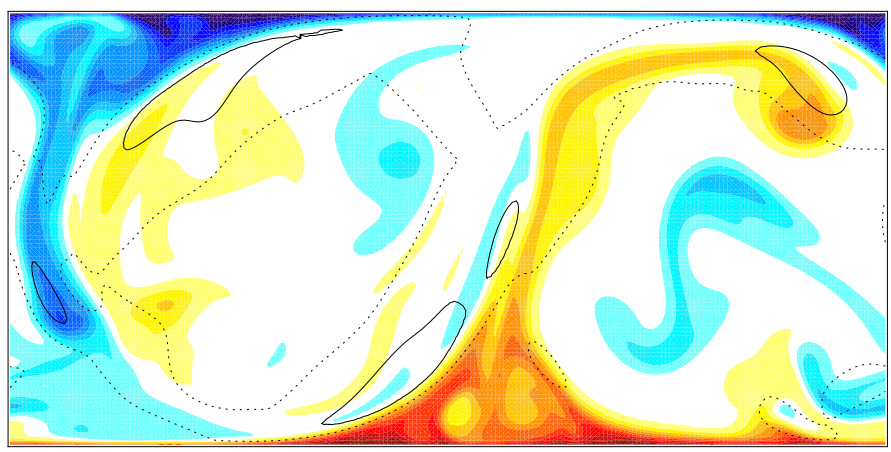

Figure 10. Potential temperature perturbations of Rayleigh-Bénard convection after 1000 time units calculated using explicit and IMEX advection with different time-steps. The dotted contour show line indicates the Courant number $c = 1$, and larger Courant numbers are shown every 0.5.

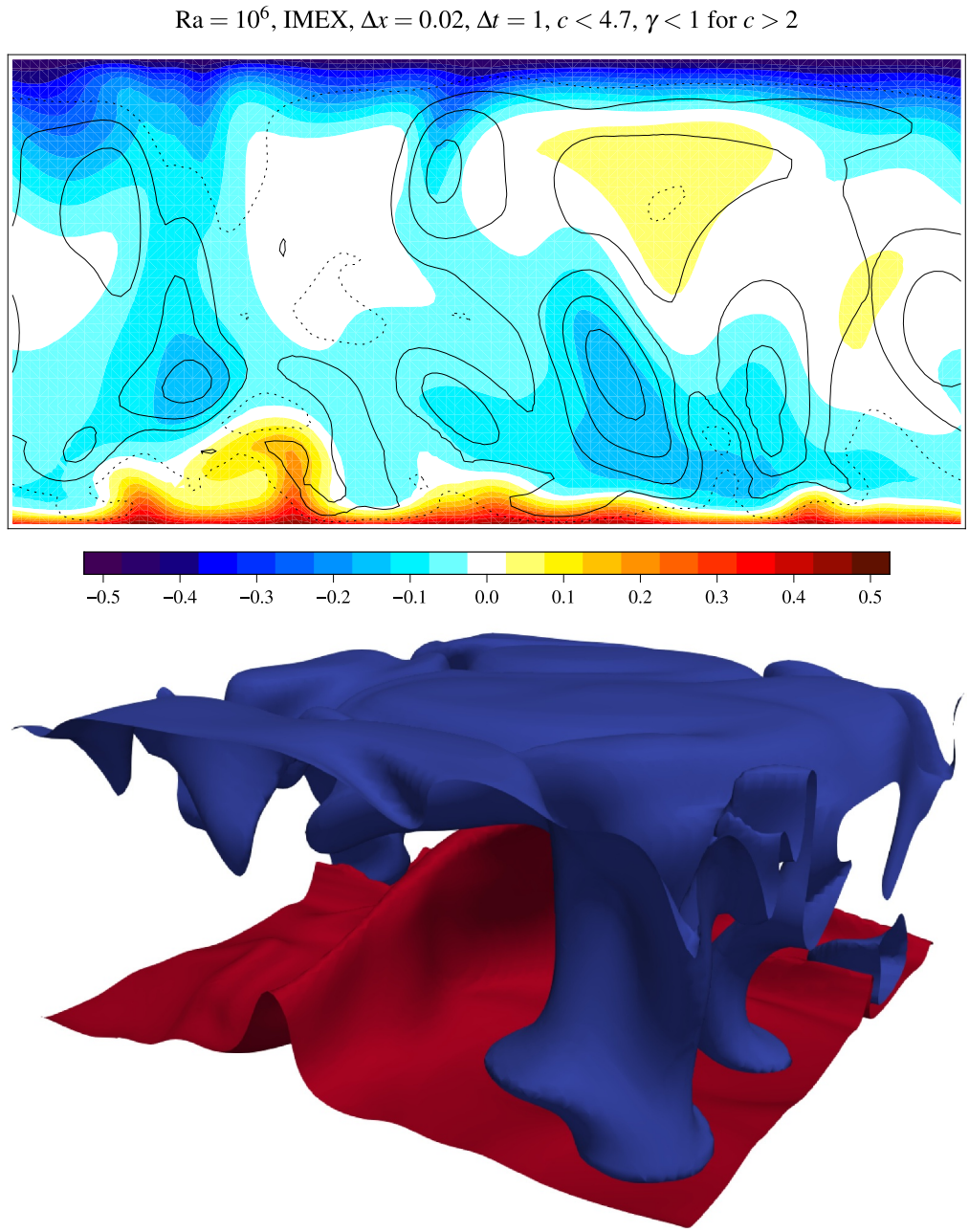

Figure 11. Potential temperature perturbations at 1000 time units from the 3D simulation Rayleigh-Bénard convection. The top panel shows a cross sections with the dotted contour line indicating the Courant number $c = 1$, and larger Courant numbers are contoured every 0.5. The bottom panel shows iso-surfaces of $\theta' = \pm 0.1$.

simulations of two dimensional convection using different spatial resolutions, and using explicit advection. The time-step scales with spatial resolution so that the maximum Courant number is around 0.5. All three resolutions show a spin up followed by oscillations in Nusselt number as the plume meanders. The dotted lines are time averages. The highest resolution produces the middle value of Nusselt number and the largest oscillations. The simulations are not converged but have similar behavior.

The intermediate spatial resolution ($\Delta x = 0.02$) is used to compare time-step size and the impact of adaptive implicit advection. The bottom panel of Figure 12 shows the Nusselt number averaged over the top and bottom boundaries for $\Delta x = 0.02$. The Nusselt number averaged just at the boundaries oscillates less than the fluid averaged Nusselt number so time averages are not needed. The spin up and time average Nusselt number is not

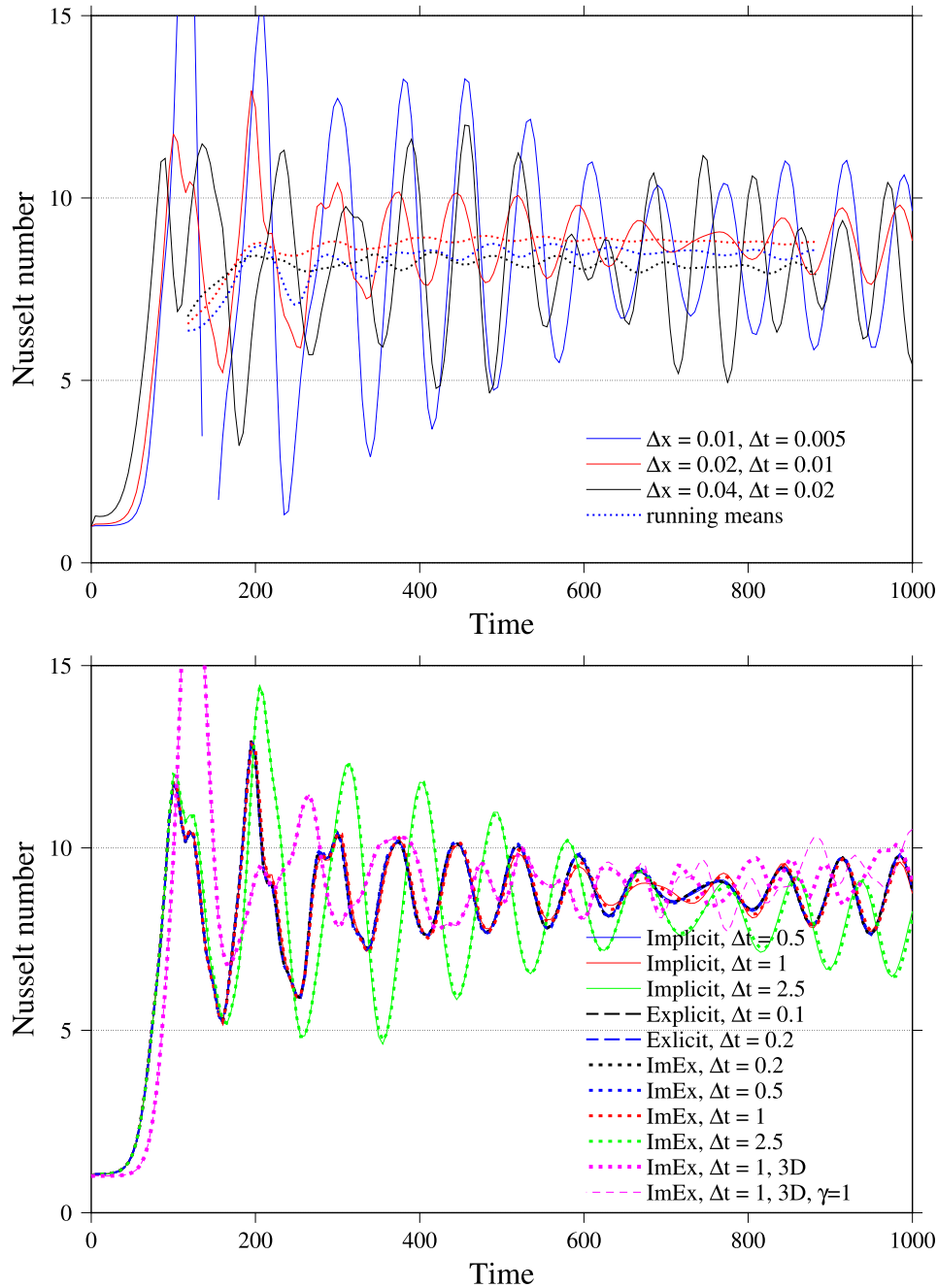

Figure 12. The top panel shows the domain averaged Nusselt number for simulations of 2D Rayleigh-Bénard convection with Ra $= 10^6$ using explicit advection and different spatial resolutions and time-step scaling with spatial resolution. The continuous lines are domain averages every 5 time units. The dotted lines are averaged over 20 sets of 5 time units. The bottom panel shows Nusselt numbers averaged over the top and bottom boundaries of 2D and 3D domains every 5 time units for simulations all using spatial resolution of 0.02.

sensitive to time-step or time-stepping method while the amplitude and period of the oscillations is sensitive to the time-step but much less sensitive to the time-stepping method. For time-steps of $\Delta t = 2.5$ time units and larger, ($c > 10$), the phase and period of the oscillations is noticeably different from the smaller time-step simulations. The Nusselt numbers of the 3D simulations are also displayed, in the lower panel of Figure 12, showing less regular oscillations but a similar mean Nusselt number and similar magnitude oscillations. 3D simulations with $\gamma \leq 1$ and with $\gamma = 1$ compared in Figure 12 confirm the small impact of using $\gamma < 1$ locally.

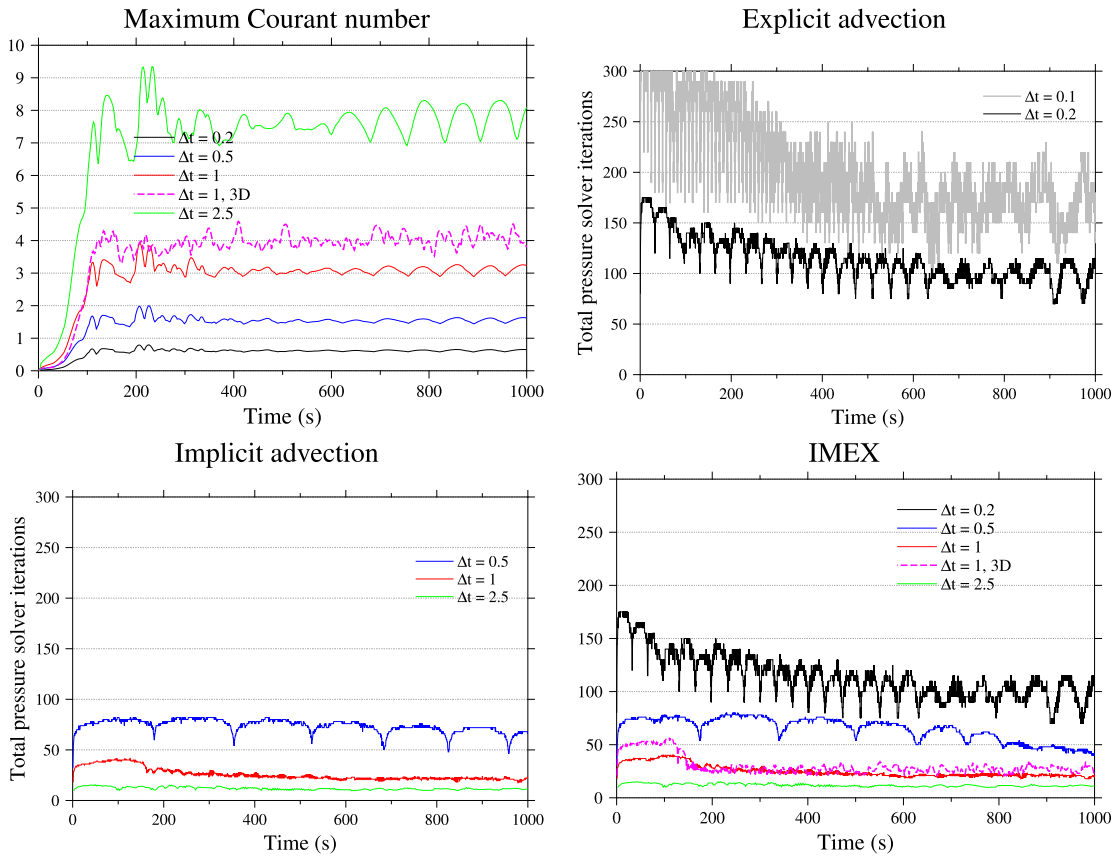

Figure 13. Maximum Courant number and total number of pressure solver iterations per unit simulated time for the solutions of Rayleigh-Bénard convection with $\mathrm{Ra} = 10^6$ using $\Delta x = 0.02$.

Again, the adaptive implicit time-stepping is behaving as required, enabling Courant numbers significantly larger than one in a fraction of the domain, without detrimental effects on accuracy.

The maximum Courant number as a function of time for the adaptively implicit (IMEX) solutions for a range of time-steps is shown in Figure 13, along with the number of iterations of the pressure solver per unit time for each time-stepping type and each time-step, all for the middle spatial resolution ($\Delta x = 0.02$). The 3D simulation has larger maximum Courant numbers than the 2D simulation with the same time-step, due to the stronger updrafts in the plumes.

For each time-stepping type, the number of pressure solver iterations per unit time reduces as the time-step increases, indicating that implicit and adaptively implicit time-stepping is cost effective for increasing time-steps. The 3D IMEX simulation uses slightly more iterations that the corresponding 2D simulation, likely because the maximum Courant numbers are higher.

3.3. Stably Stratified Flow

Strongly stratified flow introduces an additional complexity because gravity waves can be fast, so they are also treated implicitly. Two two-dimensional test cases with stratification are used; strongly stratified, near hydrostatic flow over a 1 m hill (Melvin et al., 2010) and flow over a mountain range (Schär et al., 2002).

3.3.1. Flow Over a 1 m Hill

This test case is defined by Melvin et al. (2010) and is usually run with $N\Delta t < 1$ where N is the Brunt–Väisälä frequency. The time-step limit for treating gravity waves explicitly is $N\Delta t = 1$ for forward-backward or RK2 time-stepping. This test has strong stratification so that the time-step can be increased to give $N\Delta t > 1$ in order to demonstrate the benefits of implicit treatment of gravity waves.

Table 5
Time-Steps and Resulting Maximum Courant Numbers and $N\Delta t$ for Simulations of Flow Over a 1 m Hill Using Adaptively Implicit (IMEX) Time-Stepping for Advection

Δt (s)	Max c	$N\Delta t$
20	0.2	0.39
40	0.4	0.78
100	1	1.95
200	2	3.92
500	5	9.80
1000	10	19.6

The hill has profile

$$h(x) = \frac{a^2}{x^2 + a^2}, \tag{49}$$

where $a = 10$ km in a domain 50 km deep and 240 km wide (centered on $x = 0$) with rigid top and bottom boundaries and periodic left and right boundaries. A wave absorbing layer is applied in the top 20 km with damping coefficient $\overline{\mu}\Delta t = 0.3$ (term $-\overline{\mu}w$ is added to the RHS of the w equation). The grid spacing is $\Delta x = 2$ km and $\Delta z = 250$ m. The initial wind is 20 m/s in the x-direction and the initial temperature is uniformly 250 K with the Exner pressure in discrete hydrostatic balance. The time-steps and resulting maximum Courant numbers and $N\Delta t$ for simulations which all use adaptively implicit (IMEX) time-stepping for advection are shown in Table 5.

The vertical velocity after 15,000 s for time-steps between $\Delta t = 20$ s and $\Delta t = 500$ s are shown in Figure 14 using $\gamma < 1$ for $c > 2$ as defined in Table 1. For Courant numbers up to two, the results are similar to those of, for example, Melvin et al. (2010). As the time-step increases beyond $c = 2$, the waves decrease in amplitude due to the reduced high-order spatial correction ($\gamma < 1$). The adaptively implicit time-stepping is behaving as required, stabilizing the solution for large time-steps. This simulation is stable and accurate for $\Delta t = 500$ s when using $\gamma = 1$ (bottom panel of Figure 14), but this is not recommended due to spurious results in the Schär mountain range case (Section 3.3.2). The simulation is unstable for $\Delta t = 1000$ s which is due to a combination of the large horizontal Courant number and large stratification. Simulations with time-steps this large can be stabilized by using more outer iterations per time-step but this increases cost and so these results are not presented.

The number of pressure solver iterations per 20 s of simulated time for simulations using each time-step is shown in Figure 15. As with the simulations of buoyant flows, increasing the time-step decreases the number of pressure solver iterations per 20 s of simulated time (although the number of pressure iterations per time-step increases) demonstrating the cost-effectiveness of implicit advection.

3.3.2. Flow Over Schär Mountain Range

The Schär et al. (2002) test with flow over a mountain range is useful to test the adaptive implicit time-stepping through grid cells that are distorted due to orography, which effectively increases the Courant number as defined in Equation 27. The mountain range is defined as

$$h(x) = h_m \exp\left[-\left(\frac{x}{a}\right)^2\right] \cos^2\frac{\pi x}{\lambda}, \tag{50}$$

$$h_m = 250 \text{ m}, \; a = 5 \text{ km}, \; \lambda = 4 \text{ km}. \tag{51}$$

Following Melvin et al. (2010) we use a domain of 330 km $\times$ 100 km, $\Delta x = \Delta z = 0.5$ km, and an absorbing layer in the top 10 km of the domain with damping coefficient $\overline{\mu}\Delta t = 1.2$. A basic terrain following grid is used, as defined in Klemp (2011), with periodic boundary conditions in the x-direction and zero flux boundary conditions at the top and bottom. The air is frictionless and the initial conditions consist of a wind of 10 ms^{-1} in the x-direction, a surface temperature of 288 K and stratification with $N = 0.01$ s^{-1} in hydrostatic balance.

Melvin et al. (2010) use a time-step of 8 s for this test, giving a Courant number of 0.2. Our simulations use time-steps of 8, 40, 120, and 240 s with adaptively implicit time-stepping. Contours of vertical velocity are shown in Figure 16. The 120 and 240 s solutions have $N\Delta t > 1$ and so are only stable because gravity waves are treated implicitly. The standard simulations use $\gamma < 1$ for $c > 2$ as defined in Table 1. For the two smaller time-steps, grid scale oscillations are evident downstream of the mountain, related to the co-location of pressure and velocity in this spatial discretization. These oscillations are damped when using the two larger time-steps. This is consistent with the projection scheme, applying some staggering in the pressure equation (Rhie & Chow, 1983) which damps the computational mode effectively when fast waves are not resolved. As the time-step increases beyond $c = 1$ and beyond $N\Delta t = 1$, the mountain waves become damped. This test can be run stably with $\gamma = 1$ (full

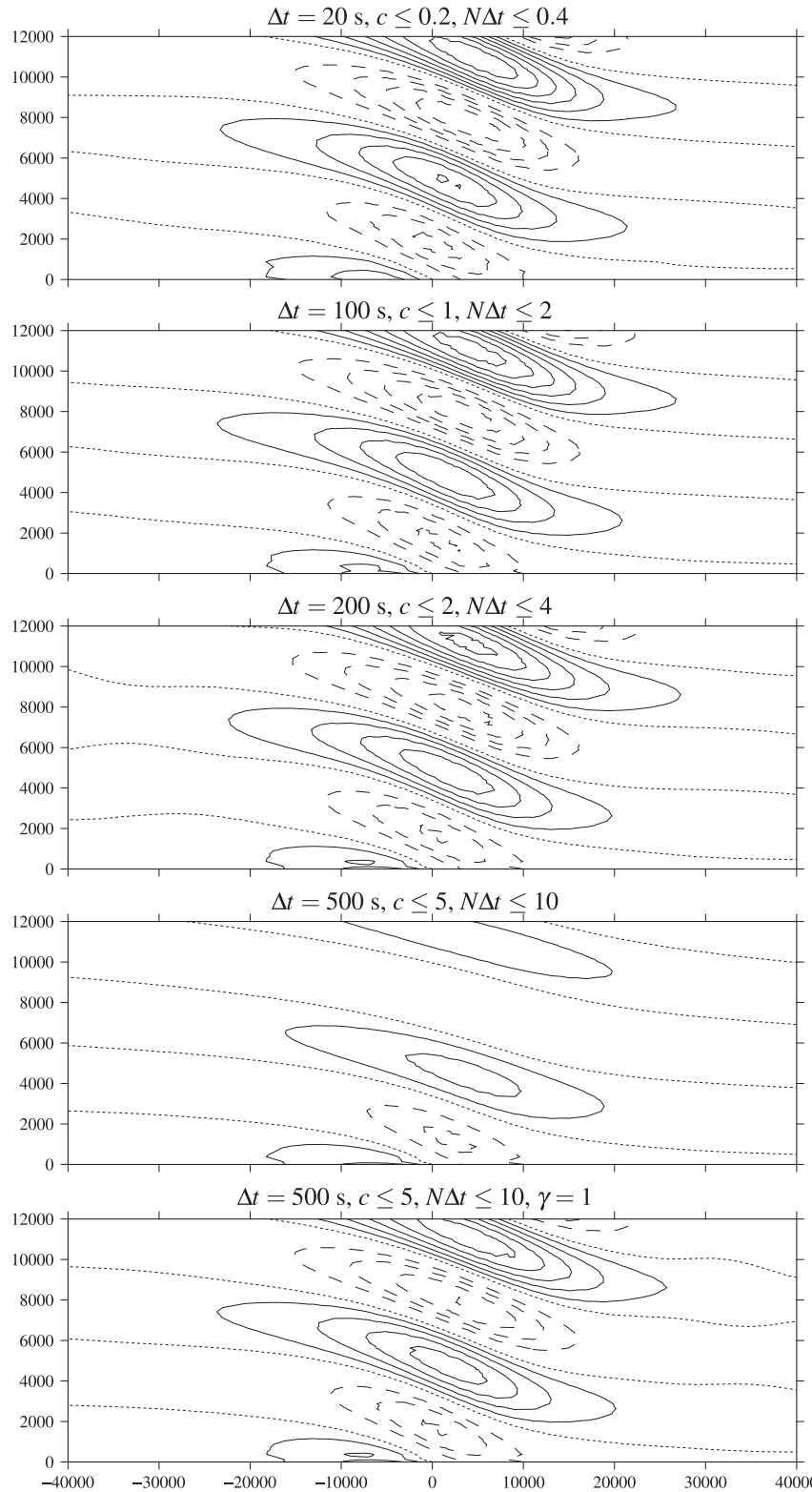

Figure 14. Vertical velocity after 1.5×10^4 seconds for stably stratified flow over a 1 m hill. Contours every 5×10^{-4}ms^{-1}, zero contour dotted. As the time-step increases, the accuracy reduces but stability is maintained since $\gamma < 1$ for $c > 2$.

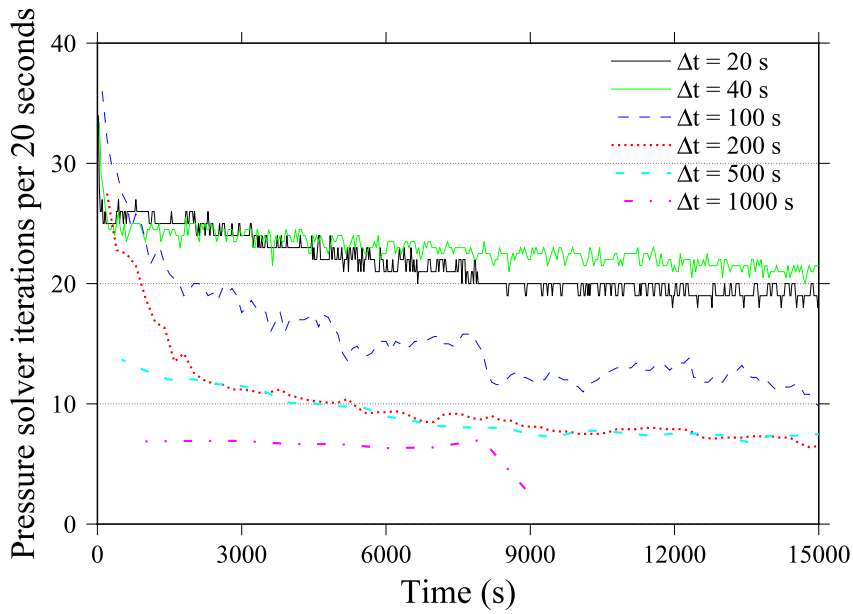

Figure 15. Total number of pressure solver iterations per 20 s of simulated time for the IMEX simulations of stratified flow over a 1 m hill. Taking larger time-steps means fewer iterations in the pressure solver in total. The simulation with the largest time-step $\Delta t = 1000$ s is not stable when using just two outer iterations per time-step.

cubic spatial correction for all Courant numbers), giving the results in the bottom panels of Figure 16. At $\Delta t = 240$ s, spurious features are visible where the undamped gravity waves generated by the mountain interact with the acoustic waves that circulate the domain, forced by the initial condition shock. Spurious features such as these are the reason for using $\gamma < 1$ for $c > 2$.

The number of pressure solver iterations per 40 s of simulated time for the adaptively implicit solution of flow over the Schär mountain range are shown in Figure 17. Taking larger time-steps means fewer iterations in the pressure solver in total, as with the other test cases.

4. Summary and Conclusions

Adaptively implicit advection uses implicit time-stepping where the Courant number is above one (or thereabouts) and standard explicit time-stepping elsewhere. We presented an adaptively implicit advection scheme with the following properties:

1. Accuracy and cost comparable with explicit time-stepping where the Courant number is less than 1 (in practice, we use a threshold of 0.8).
2. Second- or third-order accuracy for Courant numbers up to 2.
3. Stable and at least first-order accurate for Courant numbers larger than 2. The advection scheme is provably monotonic for all Courant numbers and this is demonstrated with linear advection test cases.
4. Stable solutions with large Courant numbers are also achieved solving the fully compressible Navier-Stokes equations using a combination of implicit treatment of gravity and acoustic waves with the adaptively implicit advection.
5. Given the availability of a first-order monotonic solution, FCT can be used with the adaptively implicit advection. In the methods-of-lines approach, a quasi-cubic upwind spatial discretization is combined with the two-stage implicit-explicit Runge-Kutta time-stepping using off-centering and implicitness that varies in space and time.
6. The adaptively implicit advection is suitable for a variety of mesh structures. It is demonstrated on cubed-sphere, hexagonal and latitude-longitude meshes of the sphere and terrain-following meshes over orography.

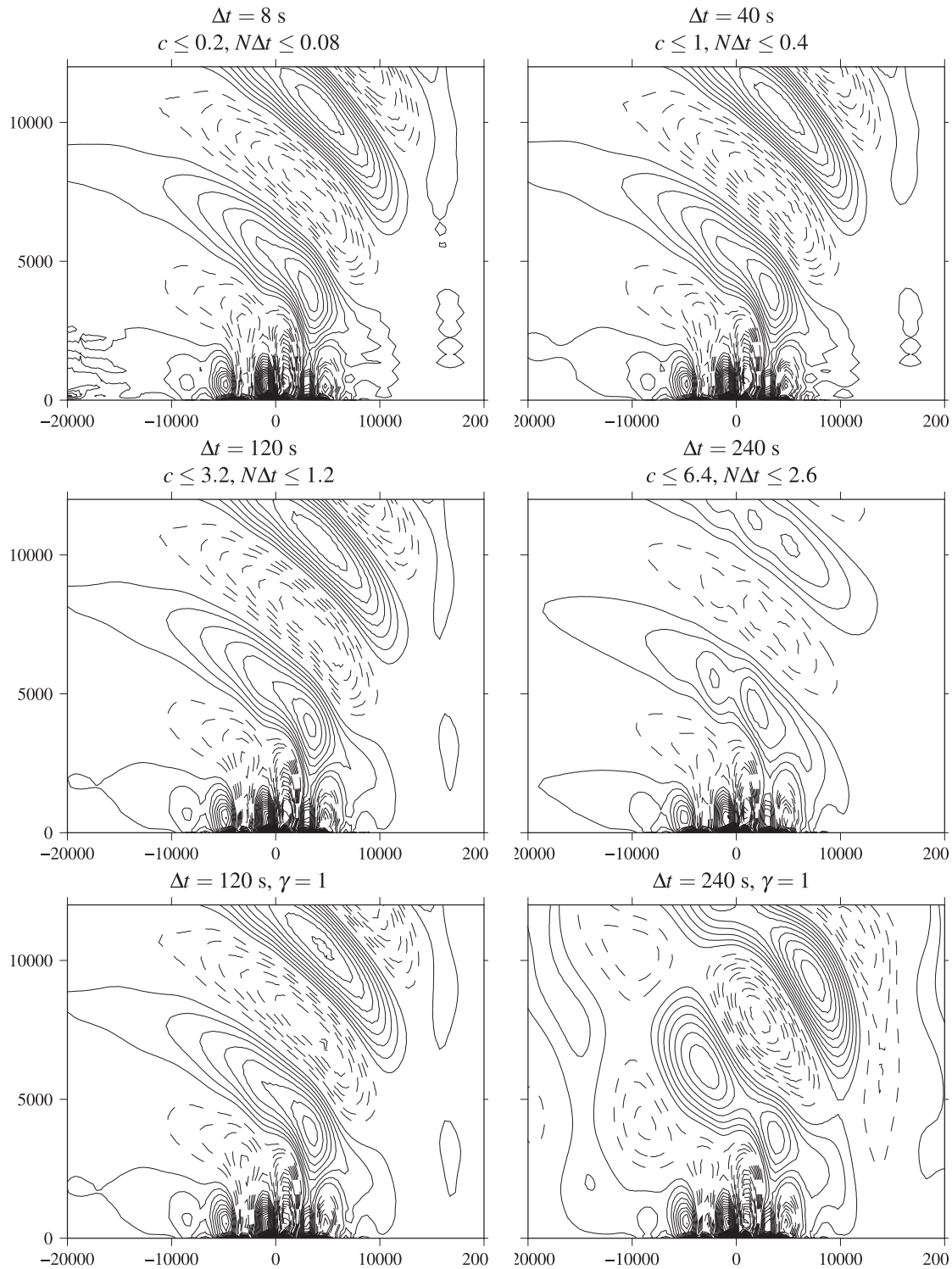

Figure 16. Vertical velocity after 1.8×10^4 seconds for flow over Schär mountains using IMEX advection. Contours every 0.05 ms^{-1}. Grid-scale oscillations associated with this particular co-located method contaminate the $\Delta t = 40$ s and $\Delta t = 8$ s results.

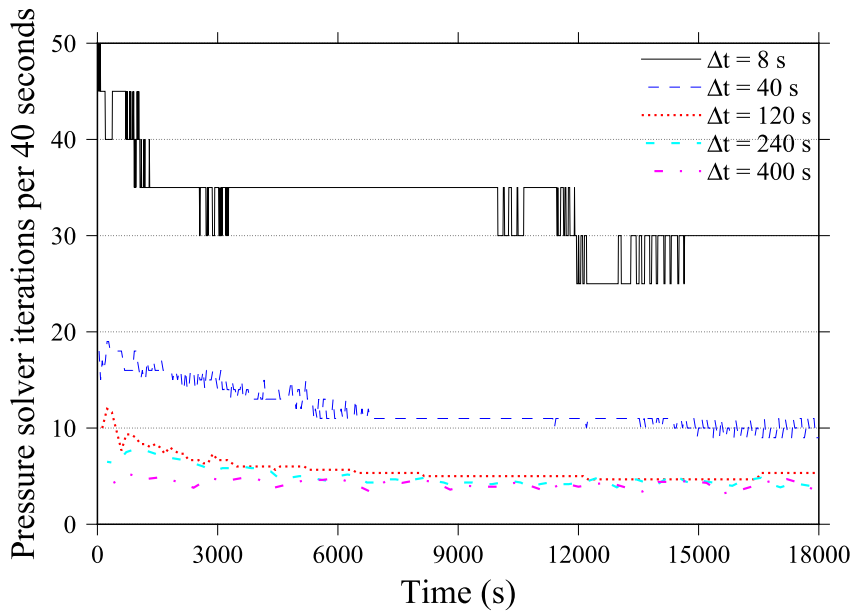

Figure 17. Total number of pressure solver iterations per 40 s of simulated time for the IMEX simulations of flow over the Schär mountain range. Taking larger time-steps means fewer iterations in the pressure solver in total.

7. Exact local conservation is achieved by defining parameters such as the spatially varying temporal off-centering at faces between grid cells, and ensuring that these spatially varying parameters are inside the divergence of the transport term.
8. Multi-tracer efficiency has not been demonstrated, but should be possible with adaptively implicit advection because the same preconditioner can be used for each tracer being transported, after which, only one solver iteration is needed for transporting each tracer.
9. Good parallel scaling has not been demonstrated here, but again, should be possible because the implicit parts of the solution use only nearest neighbor communication, since order of accuracy is reduced to first-order where the Courant number is large.
10. Adaptively implicit advection is demonstrated to be effective using just one solver iteration per application of the advection operator. Therefore, the cost of the advection does not scale with the Courant number. When used with a solution of the Euler or Navier-Stokes equations, more iterations are needed every time-step to solve the Helmholtz (pressure) equation for large time-steps. However the number of iterations to solve the pressure equation scales slower than linearly with the Courant number so cost savings are always made when the time-step is increased.

In conclusion, adaptively implicit time-stepping for advection, including in the fully compressible Navier-Stokes equations, exhibits efficiency, stability and accuracy where needed across a range of test cases. This enables the use of long time-steps which can dramatically reduce computational cost with only a small impact on accuracy. Further research is needed to explore parallel scaling aspects and application in the context of other 3D tests, as well as realistic weather and climate models.

Appendix A: Mathematical Notation

The notation used in the paper is listed in Table A1. Some notation is only used in individual sections and defined close to where it is used and so is not repeated in Table A1.

Table A1
Mathematical Notation That Is Used in More Than One Section

Physical properties			
Tracer	ψ	Source term of ψ	S_ψ
Density	ρ	Diffusion coefficient	K
Velocity	$\mathbf{u}$	Thermal diffusivity	κ
Vertical velocity component	w	Kinematic viscosity	ν
Horizontal velocity	$\mathbf{v}$	Exner pressure	π
Potential temperature	θ	Gas constant	R
Nusselt number	Nu	Brunt–Väisälä frequency	N
Rayleigh number	Ra	Acceleration due to gravity	$\mathbf{g}$
Discretization related		Courant number	c
Mass flux	ϕ	Amplification factor	$\mathcal{A}$
Volume flux	U_f	Normalized RMS error norm	ℓ_2
Face area vector	$\mathbf{S}_f$	Surface normal gradient	∇_S
Cell volume	$\mathcal{V}$	Non-orthogonal correction	∇_{noc}
Label for a cell	C	Interpolation from cells to faces	$\{\}_f$
Label for a neighbor cell	N	Reconstruction of cell values from faces	$\{\}_C$
Upwind subscript label	u	Hexagonal grid n	HRn
Downwind subscript label	d	Cubed-sphere grid n	Cn
Label for a face	f	Horizontal resolution	Δx
Time-step	Δt	Vertical resolution	Δz
High-order	HO	Temporal off-centering	α
High-order correction	HOC	Implicit flag	β
Outer iteration counter	k	High-order flux limiter	γ
Note that k is wavenumber in Section 2.3			
Vector from cell center to cell center over face f			$\mathbf{d}_f$
Diagonal matrix for the implicit conservation equation			A
Off-diagonal matrix for the implicit conservation equation			H
RHS of the matrix equation for the implicit conservation equation			R and T

Appendix B: Overview of OpenFOAM Spatial Discretization

The spatial discretization is composed from a selection of OpenFOAM 11 finite volume operators for arbitrary meshes (OpenFOAM, accessed 2024) and a simple quasi-cubic upwind advection scheme described in Section 2.1. This section describes the spatial discretization of a generic variable ψ for terms other than advection.

Using Gauss's theorem, cell gradients of ψ in volume $\mathcal{V}$ are calculated as

$$\nabla\psi \approx \frac{1}{\mathcal{V}}\int_{\mathcal{V}} \nabla\psi \, \mathrm{d}\mathcal{V} = \frac{1}{\mathcal{V}}\int_S \psi \mathrm{d}\mathbf{S} \approx \frac{1}{\mathcal{V}}\sum_{\text{faces}} \{\psi\}_f \mathbf{S}_f, \tag{B1}$$

where operator $\{\}_f$ means linear interpolation from cells to faces

$$\{\psi\}_f = \lambda\psi_C + (1-\lambda)\psi_N, \tag{B2}$$

where λ is the linear interpolation weight from points $\mathbf{x}_C$ and $\mathbf{x}_N$ (the cell centers) to $\mathbf{x}_f$ (the face center)

$$\lambda = \frac{|\mathbf{x}_N - \mathbf{x}_f|}{|\mathbf{x}_N - \mathbf{x}_C|}. \tag{B3}$$

The discretization in this paper ignores the first-order skewness error that occurs when the intersection between points and the face does not co-incide with the face center. Correcting this error does not have a noticeable influence on the results in this paper. The gradients are calculated at faces by linearly interpolating cell gradients onto faces and correcting the component normal to the face using the simple two-point difference

$$\nabla_f\psi = \underbrace{\{\nabla\psi\}_f}_{\substack{\text{full gradient}\\ \text{interpolated}}} + \underbrace{(\psi_N - \psi_C)\frac{\mathbf{x}_N - \mathbf{x}_C}{|\mathbf{x}_N - \mathbf{x}_C|^2}}_{\text{two-point difference}} - \underbrace{\{\nabla\psi\}_f \cdot \frac{\mathbf{x}_N - \mathbf{x}_C}{|\mathbf{x}_N - \mathbf{x}_C|}}_{\substack{\text{removal of component included}\\ \text{from two-point difference}}}. \tag{B4}$$

Scalar valued, surface normal gradients, $\nabla_S\psi = \mathbf{S}_f \cdot \nabla\psi$, use a non-orthogonal correction (noc) of the two-point difference, based on the $\mathbf{S}_f$ component of Equation B4

$$\nabla_S\psi = \underbrace{\frac{\psi_N - \psi_C}{|\mathbf{d}_f|}|\mathbf{S}_f|}_{\nabla_2} + \underbrace{\{\nabla\psi\}_f \cdot \mathbf{S}_f - \{\nabla\psi\}_f \cdot \mathbf{d}_f}_{\nabla_{\text{noc}}}, \tag{B5}$$

where $\mathbf{d}_f = \mathbf{x}_N - \mathbf{x}_C$. The first term of Equation B5 is the two-point difference, $\nabla_2\psi$, and the second two terms are the non-orthogonal correction, $\nabla_{\text{noc}}\psi$. The two point difference can be treated implicitly and the non-orthogonal correction is always treated explicitly. Note that ∇ is used as a gradient operator even when it only refers to a component of the gradient.

There are two relevant spatial averaging operators denoted by the symbol $\{\}_C$ which are the reconstruction of cell center vectors, $\mathbf{a}_C$, from face normal vector $A_S = \mathbf{a}_f \cdot \mathbf{S}_f$, and averaging of face scalar values, Ψ_f, to cell centers, defined as

$$\mathbf{a}_C = \{A_S\}_C = \left(\sum_{\text{faces}} \mathbf{S}_f\mathbf{S}_f^T\right)^{-1} \sum_{\text{faces}} \mathbf{S}_f A_S, \tag{B6}$$

$$\left\{\psi_f\right\}_C = \sum_{\text{faces}} |\mathbf{S}_f|\psi_f \Big/ \sum_{\text{faces}} |\mathbf{S}_f|, \tag{B7}$$

where $\sum_{\text{faces}}\mathbf{S}_f\mathbf{S}_f^T$ is a 3×3 tensor for each cell.

Appendix C: Solution of the Fully Compressible Navier-Stokes Equations

The potential temperature and momentum Equations 39 and 40 are first solved keeping the right hand side fixed and with the advection and diffusion terms solved adaptively implicitly. Next, the advection and diffusion terms are held fixed and Equations 39 and 40 are combined with the continuity Equation 38 and the equation of state Equation 42 to form a Helmholtz equation for the perturbation Exner pressure, π'. Prognostic variables, $\mathbf{u}$, θ' and ρ are all at cell centers, along with π'. Mass fluxes through faces, ϕ, are calculated every time-step, with ρ and $\mathbf{u}$ linearly interpolated from cell centers onto faces in order to initialize ϕ.

In order to describe the solution algorithm for each time-step, we index the outer iterations with k, as in Section 2.2.2. At the beginning of each time-step, each variable at $k = 0$ is set to the old time level value, n.

C1. Explicit Continuity Update for Consistency

The continuity equation is combined with the equation of state, potential temperature and momentum equations to form a Helmholtz equation in order to treat acoustic and gravity waves implicitly (Section C4). However, this process does not converge to machine precision, so the resulting density and mass fluxes do not exactly solve the continuity equation. This means that the flux form solutions of density weighted variables (potential temperature and velocity) are not consistent with continuity. In order to fix this, density is updated explicitly using the fluxes from the Helmholtz equation (Equation C17) before advecting mass weighted variables. Therefore, the first step of the outer iteration, starting from $k = 1$, is to update ρ from the most recent flux, ϕ.

$$\rho^k = \rho^{(n)} - \frac{\Delta t}{\mathcal{V}} \sum_f (1-\alpha)\phi^{(n)} - \frac{\Delta t}{\mathcal{V}} \sum_f \alpha \phi^{k-1}. \tag{C1}$$

This is an explicit update of a transport equation with a large Courant number, which might be considered cause for concern. However the fluxes used are implicit solutions of the continuity equation (Section C4). Therefore the solution of Equation C1 is a small correction and so does not lead to instability.

The mass fluxes, ϕ, that are used in the solution of Equation C1 for ρ are the same as the mass fluxes and density that are used in all advection-diffusion equations of the form Equation 11 and solved in the form Equation 18. This gives consistency with continuity and uniform ψ fields are maintained.

C2. Adaptively Implicit Solution of the Potential Temperature Equation

Next the θ'' equation is solved to find θ''^k as described in Section 2.2, with the advection treated adaptively implicitly and the diffusion term treated implicitly. The θ'' equation is put into the form Equation 18 with $K = \kappa$, with $A_{\theta''}$, $H_{\theta''}$ and $R_{\theta''}$ as in Equations 21–23, and with

$$S_{\theta''}^{(n)} = -\rho^{(n)} w^{(n)} \frac{d\overline{\theta}}{dz} \qquad S_{\theta''}^{k-1} = -\rho^k w^{k-1} \frac{d\overline{\theta}}{dz}. \tag{C2}$$

Note that w from a previous iteration is used. This implies that gravity waves are not treated implicitly in the solution of the θ'' equation. This comes in the solution of the momentum equation, described in Section C3.

Solution of Equation 18 for θ'' gives θ''^k. From this we linearly interpolate to get θ''^k_f and add $\overline{\theta}$ to get θ^k and θ^k_f.

C3. Adaptively Implicit Solution of the Momentum Equation

Before the solution of the Helmholtz equation (Section C4), the momentum equation is solved with advection treated adaptively implicitly, diffusion treated implicitly, gravity waves treated implicitly and the pressure gradient held fixed from the previous iteration. Without implicit gravity waves, the momentum equation fits into the advection-diffusion equation form of Equation 11 with

$$S_{\mathbf{u}} = -\rho \left\{ \frac{\{\theta''\}_f}{\overline{\theta}} \mathbf{g} \cdot \mathbf{S}_f + c_p \{\theta\}_f \nabla_S \pi'' \right\}_C. \tag{C3}$$

In order to treat gravity waves implicitly, part of the contribution to θ''_f from w is removed so that it can be combined with w on the left hand side of the momentum equation. This leaves a modified θ''_f which is stored on faces and we will call ϑ

$$\vartheta = \overline{\theta} + \vartheta'' = \overline{\theta} + \theta''^k_f + \alpha \Delta t w^k_f \frac{\partial \overline{\theta}^k}{\partial z}. \tag{C4}$$

θ''^k_f and θ^k_f are replaced by ϑ^k in Equation C3 using Equation C4 giving

$$S_{\mathbf{u}} = -\rho\alpha\Delta t w \frac{\partial\theta}{\partial z}\left(\frac{\mathbf{g}}{\bar{\theta}} + c_p\nabla\pi'\right) - \rho\left\{\frac{\vartheta'}{\bar{\theta}}\mathbf{g}\cdot\mathbf{S}_f + c_p\vartheta\nabla_S\pi'\right\}_C. \tag{C5}$$

In order to treat gravity waves implicitly, vertical velocity, w, and horizontal velocity, $\mathbf{v}$, are treated differently, with the first term of Equation C5 being moved to A_w for the w equation. The equations for $\mathbf{v}$ and w are of the form Equation 18 with $R_{\mathbf{v}}$ and R_w as in Equation 23 $H_{\mathbf{v}}$ and H_w as in Equation 22, $A_{\mathbf{v}}$ as in Equation 21 and

$$A_w = A_\psi - \rho^k\Delta t\frac{\partial\theta^k}{\partial z}\left\{\alpha^2\left(\frac{\mathbf{g}\cdot\mathbf{S}_k}{\bar{\theta}_f} + c_p\nabla_S\pi'^{k-1}\right)\cdot\mathbf{k}\right\}_C, \tag{C6}$$

$$S_{\mathbf{v}}^{k-1} = -\rho^k\left\{c_p\vartheta_f^k\nabla_S\pi'^{k-1}\right\}_C, \tag{C7}$$

$$S_{\mathbf{v}}^{(n)} = -\rho^{(n)}\left\{c_p\theta_f^{(n)}\nabla_S\pi'^{(n)}\right\}_C, \tag{C8}$$

$$S_w^{k-1} = -\rho^k\left\{\frac{\vartheta_f'^k}{\bar{\theta}}\mathbf{g}\cdot\mathbf{S}_f + c_p\theta_f^k\nabla_S\pi'^{k-1}\right\}_C, \tag{C9}$$

$$S_w^{(n)} = -\rho^n\left\{\frac{\theta_f'^{(n)}}{\bar{\theta}}\mathbf{g}\cdot\mathbf{S}_f + c_p\theta_f^{(n)}\nabla_S\pi'^{(n)}\right\}_C. \tag{C10}$$

Solution of Equation 18 for $\mathbf{v}$ and w using Equations C6–C10 gives us temporary values of $\mathbf{v}^k$ and w^k which will be updated after the solution of the Helmholtz equation (Section C4).

C4. The Helmholtz Equation for Exner Pressure

Construction of the Helmholtz equation for π' involves writing the mass flux, ϕ, and the density, ρ, as a linear function of π' and substituting both into the continuity equation.

To express ϕ as a linear function of π', we first rewrite the velocities without contributions from the new time level pressure gradient or gravity

$$\tilde{\mathbf{v}} = \frac{H_v\mathbf{v}^k - R_v}{A_v} \quad \tilde{w} = \frac{H_w w^k - R_w}{A_w}. \tag{C11}$$

To express ϕ in terms of $\tilde{\mathbf{v}}$ and $\tilde{w}$, we interpolate $\tilde{\mathbf{v}}$ and $\tilde{w}$ onto the faces, add the contribution from the new time level pressure gradient and gravity (note π'^k not known yet), multiply by density interpolated onto faces and take the dot product with $\mathbf{S}_f$

$$\phi^k = \rho_f\begin{Bmatrix}\tilde{\mathbf{v}}\\ \tilde{w}\end{Bmatrix}_f\cdot\mathbf{S}_f - \alpha\Delta t\begin{Bmatrix}\frac{\rho^k}{A_v} & 0\\ 0 & \frac{\rho^k}{A_w}\end{Bmatrix}_f\left(\frac{\vartheta'}{\bar{\theta}_f}\mathbf{g} + c_p\vartheta\nabla\pi'^k\right)\cdot\mathbf{S}_f. \tag{C12}$$

This has similarities to the Rhie and Chow (1983) method.

To express ρ as a linear function of π' we write

$$\rho = \rho^k + \rho', \quad \pi'^k = \pi'_\rho + \pi'', \tag{C13}$$

where ρ' is the small increment that updates ρ^k to be consistent with π'^k and π'_ρ satisfies the continuity equation with ρ^k

$$\rho^k = \frac{p_r}{R\theta}(\overline{\pi} + \pi'_\rho)^{\frac{c_v}{R}}, \tag{C14}$$

and π'' is the small increment that takes π' from π'_ρ to π'^k. Using the linearization

$$\left(1 + \frac{\pi''}{\overline{\pi} + \pi'_\rho}\right)^{\frac{c_v}{R}} \approx 1 + \frac{c_v}{R}\frac{\pi''}{\overline{\pi} + \pi'_\rho}, \tag{C15}$$

we get the linearized equation of state

$$\rho = \rho^k\left(1 + \frac{c_v}{R}\frac{\pi''}{\overline{\pi} + \pi'_\rho}\right), \tag{C16}$$

which can be substituted into the continuity equation to give a Helmholtz equation for $\pi'^k = \pi'_\rho + \pi''$

$$\frac{\rho^k \frac{c_v}{R}}{\overline{\pi} + \pi'_\rho}\frac{\pi'^k - \pi'_\rho}{\Delta t} + \frac{\rho^k - \rho^{(n)}}{\Delta t} + \nabla \cdot \phi^k = 0, \tag{C17}$$

where $\phi^k(\pi'^k)$ is from Equation C12. Equation C17 is solved using the OpenFOAM multigrid solver (GAMG) with a diagonal incomplete Cholesky (DIC) smoother until the residual (the normalized volumetric mean absolute error, see WWKS23) is below a tolerance. The tolerance is 10^{-6} for the final pressure solution per time-step but capped at 0.01 times the initial residual for other solves.

Next, π'^k is used to back substitute to calculate ϕ^k from Equation C12 and to update the velocity

$$\mathbf{u}^k = \begin{pmatrix}\widetilde{\mathbf{v}}\\ \tilde{w}\end{pmatrix} - \Delta t \begin{pmatrix}\frac{\rho^k}{A_v} & 0\\ 0 & \frac{\rho^k}{A_w}\end{pmatrix}\left\{\alpha\left(\frac{\vartheta'}{\overline{\theta}_f}\mathbf{g}\cdot\mathbf{S}_f + c_p\vartheta\nabla_S\pi'^k\right)\right\}_C. \tag{C18}$$

All of the calculations in this subsection are repeated twice per outer iteration with the calculation of $\widetilde{\mathbf{v}}$ and $\tilde{w}$ updated to use the most recent $\mathbf{v}^k$ and w^k for the second iteration.

C5. Algorithm Summary at Each Time-Step

- Calculate the Courant number in cells and on faces Equations 27 and 28 and the Brunt–Väisälä frequency, N Equation 29. From these calculate the stability parameters, α, β and γ (Table 1).
- Undertake two outer (Picard) iterations:
  1. Update density, ρ, explicitly from mass fluxes, ϕ, using Equation C1.
  2. For θ', calculate the explicit source, $S_{\theta}{}'$ Equation C2, and the matrix diagonal and off-diagonal entries, A_θ Equation 21, H_θ Equation 22 and the matrix source, R_θ Equation 23 and $T_{\theta}{}'$ Equation 24.
  3. Solve the matrix equation for θ' Equation 18 using one CG iteration using a DILU preconditioner. In the final outer iteration, this is repeated twice with explicit terms updated to improve convergence.
  4. Remove the part of the θ' update related to gravity waves using Equation C4 to calculate ϑ and ϑ'.
  5. For $\mathbf{u}$, calculate the explicit source terms, $S_{\mathbf{v}}$ and S_w Equations C7 and C9 without the parts of θ' that are treated implicitly for gravity waves. Calculate the matrix diagonals, $A_{\mathbf{v}}$, A_w, with A_w modified Equation C6 to account for the implicit treatment of gravity waves. Calculate the matrix off-diagonals, $H_{\mathbf{v}}$, H_w and the matrix source terms, $R_{\mathbf{v}}$, $T_{\mathbf{v}}$, R_w and T_w using Equations 23 and 24.
  6. Solve the matrix equations for u, v and w Equation 18 using one CG iteration using a DILU preconditioner. These have pressure gradients and positive buoyancy fixed from a previous iteration.
  7. Two inner (Picard) iterations are used to solve the Helmholtz equation for π' and to update $\mathbf{u}$:

(a) Temporary values of the velocities, $\tilde{\mathbf{v}}$ and $\tilde{w}$, are calculated without the pressure gradient or gravity using Equation C11. These are used to calculate the mass flux without the pressure gradient, ϕ', from Equation C12 but without the term involving π'.
(b) ϕ', and π'_ρ from the linearized equation of state Equation C16, are substituted into the continuity equation to get the Helmholtz equation (Equation C17). This is solved implicitly for Exner perturbation, π' using the OpenFOAM multi-grid solver with an incomplete Cholesky smoother.
(c) The back-substitution step updates ϕ from π' and ϕ' using Equation C12 and $\mathbf{u}$ from the temporary velocities, $\tilde{\mathbf{v}}$ and $\tilde{w}$, using Equation C18.

- The stability parameters, α, β and γ, are only calculated once per time-step. This means that the contributions from the old time levels (terms including $1-\alpha$), only need to be calculated once per time-step. This could potentially lead to stability issues if the velocity or stable stratification were to dramatically increase within one time-step. This does not occur in the test cases in Section 3.

Appendix D: Order of Convergence of Quasi-Cubic Advection Scheme

In the deformational flow advection tests (Section 3.1.1), the quasi-cubic advection scheme together with the adaptively implicit time-stepping converges with second-order accuracy. However in a more simplified setting, and with third-order time-stepping, third-order convergence is achieved.

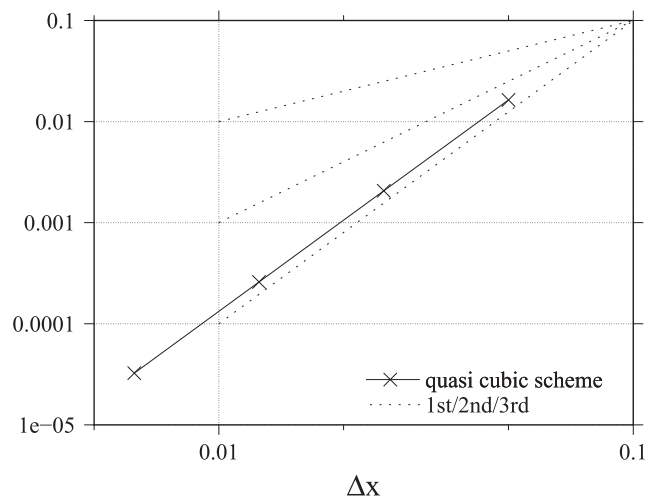

Figure D1. ℓ_2 error norm after advecting a doubly sinusoidal profile one revolution around a periodic, unit square by velocity field $(1,1,0)$ using quasi-cubic spatial discretization and RK3 time-stepping.

The initial conditions consist of a double sinusoidal profile in a unit square domain

$$\psi = \frac{1}{4}(1+\sin(2\pi x))(1+\sin(2\pi y)) \quad (x,y)\in[0,1)^2, \tag{D1}$$

which is advected in a uniform grid by a constant velocity field, $(1,1,0)$ for one time unit so that the initial conditions return to their original location. The smoothness of the velocity field and the initial conditions mean that initial conditions are set as sampled values at cell centers and velocities are sampled at face centers, rather than using third-order approximations to set cell average and face average values. Grids of size 20×20, 40×40, 80×80, and 160×160 are used with time-steps of 0.02, 0.01, 0.005, and 0.0025 time units giving a Courant number of 0.8.

The advection uses third-order Runge-Kutta time-stepping

$$\begin{aligned}\psi^1 &= \psi^{(n)} - \Delta t \nabla_{\mathrm{HO}} \cdot \mathbf{u}\psi^{(n)},\\ \psi^2 &= \psi^{(n)} - \frac{\Delta t}{4}\left\{\nabla_{\mathrm{HO}} \cdot \mathbf{u}\psi^{(n)} + \nabla_{\mathrm{HO}} \cdot \mathbf{u}\psi^1\right\},\\ \psi^{(n+1)} &= \psi^{(n)} - \frac{\Delta t}{6}\left\{\nabla_{\mathrm{HO}} \cdot \mathbf{u}\psi^{(n)} + \nabla_{\mathrm{HO}} \cdot \mathbf{u}\psi^1 + 4\nabla_{\mathrm{HO}} \cdot \mathbf{u}\psi^2\right\}.\end{aligned} \tag{D2}$$

The ℓ_2 error norm is the (normalized) root mean square error and is shown as a function of resolution in Figure D1, confirming the third-order convergence in this highly idealized setting.

Data Availability Statement

The code used to produce these results is at https://zenodo.org/doi/10.5281/zenodo.593780 (Weller, 2024a). The test cases set ups are at https://zenodo.org/doi/10.5281/zenodo.11546593 (Weller, 2024b). The code can be compiled with OpenFOAM 11 (OpenFOAM, accessed 2024) https://openfoam.org/version/11/.

Acknowledgments
Hilary acknowledges valuable discussions with James Woodfield and Amber te Winkel. PKS acknowledges that his contribution is based upon work supported by the NSF National Center for Atmospheric Research, which is a major facility sponsored by the U.S. National Science Foundation under Cooperative Agreement No 1852977.

References

Baldauf, M., Seifert, A., Förstner, J., Majewski, D., Raschendorfer, M., & Reinhardt, T. (2011). Operational convective-scale numerical weather prediction with the COSMO model: Description and sensitivities. *Monthly Weather Review*, *139*(12), 3887–3905. https://doi.org/10.1175/mwr-d-10-05013.1

Bendall, T. M., & Kent, J. (2024). Swift: A monotonic, flux-form semi-Lagrangian tracer transport scheme for flow with large courant numbers. Retrieved from https://arxiv.org/abs/2405.20006

Bryan, G., & Fritsch, J. (2002). A benchmark simulation for moist nonhydrostatic numerical models. *Monthly Weather Review*, *130*(12), 2917–2928. https://doi.org/10.1175/1520-0493(2002)130<2917:absfmn>2.0.co;2

Chen, Y., Weller, H., Pring, S., & Shaw, J. (2017). Comparison of dimensionally split and multi-dimensional atmospheric transport schemes for long time steps. *Quarterly Journal of the Royal Meteorological Society*, *143*(708), 2764–2779. https://doi.org/10.1002/qj.3125

Cullen, M., & Davies, T. (1991). A conservative split-explicit integration scheme with fourth-order horizontal advection. *Quarterly Journal of the Royal Meteorological Society*, *117*(401), 993–1002. https://doi.org/10.1002/qj.49711750106

Davies, T., Cullen, M., Malcolm, A., Mawson, M., Staniforth, A., White, A., & Wood, N. (2005). A new dynamical core for the Met Office's global and regional modelling of the atmosphere. *Quarterly Journal of the Royal Meteorological Society*, *131*(608), 1759–1782. https://doi.org/10.1256/qj.04.101

Dennis, J., Edwards, J., Evans, K., Guba, O., Lauritzen, P., Mirin, A., et al. (2012). CAM-SE: A scalable spectral element dynamical core for the community atmosphere model. *The International Journal of High Performance Computing Applications*, *26*(1), 74–89. https://doi.org/10.1177/1094342011428142

Diamantakis, M., & Váňa, F. (2022). A fast converging and concise algorithm for computing the departure points in semi-Lagrangian weather and climate models. *Quarterly Journal of the Royal Meteorological Society*, *148*(743), 670–684.

Durran, D., & Blossey, P. (2012). Implicit-explicit multistep methods for fast-wave–slow-wave problems. *Monthly Weather Review*, *140*(4), 1307–1325. https://doi.org/10.1175/mwr-d-11-00088.1

Giraldo, F., Kelly, J., & Constantinescu, E. (2013). Implicit-explicit formulations of a three-dimensional nonhydrostatic unified model of the atmosphere (NUMA). *SIAM Journal on Scientific Computing*, *35*(5), B1162–B1194. https://doi.org/10.1137/120876034

Gottlieb, S., Shu, C.-W., & Tadmor, E. (2001). Strong stability-preserving high-order time discretization methods. *SIAM Review*, *43*(1), 89–112. https://doi.org/10.1137/s003614450036757x

Harris, L. M., Lauritzen, P. H., & Mittal, R. (2011). A flux-form version of the conservative semi-Lagrangian multi-tracer transport scheme (CSLAM) on the cubed sphere grid. *Journal of Computational Physics*, *230*(4), 1215–1237. https://doi.org/10.1016/j.jcp.2010.11.001

Hortal, M. (2002). The development and testing of a new two-time-level semi-Lagrangian scheme (SETTLS) in the ECMWF forecast model. *Quarterly Journal of the Royal Meteorological Society*, *128*(583), 1671–1687. https://doi.org/10.1256/00359000260247417

Jebens, S., Knoth, O., & Weiner, R. (2011). Partially implicit peer methods for the compressible Euler equations. *Journal of Computational Physics*, *230*(12), 4955–4974. https://doi.org/10.1016/j.jcp.2011.03.015

Klemp, J. (2011). A terrain-following coordinate with smoothed coordinate surfaces. *Monthly Weather Review*, *139*(7), 2163–2169. https://doi.org/10.1175/mwr-d-10-05046.1

Kühnlein, C., Deconinck, W., Klein, R., Malardel, S., Piotrowski, Z. P., Smolarkiewicz, P. K., et al. (2019). FVM 1.0: A nonhydrostatic finite-volume dynamical core for the IFS. *Geoscientific Model Development*, *12*(2), 651–676. https://doi.org/10.5194/gmd-12-651-2019

Lauritzen, P. (2007). A stability analysis of finite-volume advection schemes permitting long time steps. *Monthly Weather Review*, *135*(7), 2658–2673. https://doi.org/10.1175/mwr3425.1

Lauritzen, P., Erath, C., & Mittal, R. (2011). On simplifying "incremental remap" -based transport schemes. *Journal of Computational Physics*, *230*(22), 7957–7963.

Lauritzen, P., Skamarock, W., Prather, M., & Taylor, M. (2012). A standard test case suite for two-dimensional linear transport on the sphere. *Geoscientific Model Development*, *5*(3), 887–901. https://doi.org/10.5194/gmd-5-887-2012

Lauritzen, P., Ullrich, P., Jablonowski, C., Bosler, P., Calhoun, D., Conley, A., et al. (2014). A standard test case suite for two-dimensional linear transport on the sphere: Results from a collection of state-of-the-art schemes. *Geoscientific Model Development*, *7*(1), 105–145. https://doi.org/10.5194/gmd-7-105-2014

Leonard, B., Lock, A., & Macvean, M. (1995). The NIRVANA scheme applied to one-dimensional advection. *International Journal of Numerical Methods for Heat and Fluid Flow*, *5*(4), 341–377. https://doi.org/10.1108/eum0000000004120

Leonard, B., Lock, A., & MacVean, M. (1996). Conservative explicit unrestricted-time-step multidimensional constancy-preserving advection schemes. *Monthly Weather Review*, *124*(11), 2585–2606. https://doi.org/10.1175/1520-0493(1996)124<2588:ceutsm>2.0.co;2

Li, J., & Dong, L. (2024). A long-time-step-permitting tracer transport model on the regular latitude-longitude grid. *Advances in Atmospheric Sciences*, *41*(3), 493–508. https://doi.org/10.1007/s00376-023-2270-z

Lin, S., & Rood, R. (1996). Multidimensional flux-form semi-Lagrangian transport schemes. *Monthly Weather Review*, *124*(9), 2046–2070. https://doi.org/10.1175/1520-0493(1996)124<2046:mffslt>2.0.co;2

Lipscomb, W., & Ringler, T. (2005). An incremental remapping transport scheme on a spherical geodesic grid. *Monthly Weather Review*, *133*(8), 2335–2350. https://doi.org/10.1175/mwr2983.1

Malardel, S., Wedi, N., Deconinck, W., Diamantakis, M., Kuehnlein, C., Mozdzynski, G., et al. (2016). A new grid for the IFS. In *ECMWF Newsletter* (Vol. 146, pp. 23–28). Retrieved from https://www.ecmwf.int/en/elibrary/80059-new-grid-ifs

May, S., & Berger, M. (2017). An explicit implicit scheme for cut cells in embedded boundary meshes. *Journal of Computational Physics*, *71*(3), 919–943. https://doi.org/10.1007/s10915-016-0326-2

Melvin, T., Benacchio, T., Shipway, B., Wood, N., Thuburn, J., & Cotter, C. (2019). A mixed finite-element, finite-volume, semi-implicit discretization for atmospheric dynamics: Cartesian geometry. *Quarterly Journal of the Royal Meteorological Society*, *145*(724), 2835–2853. https://doi.org/10.1002/qj.3501

Melvin, T., Dubal, M., Wood, N., Staniforth, A., & Zerroukat, M. (2010). An inherently mass-conserving semi-implicit semi-Lagrangian discretisation of the nonhydrostatic vertical slice equations. *Quarterly Journal of the Royal Meteorological Society*, *137*, 799–814.

Miura, H. (2007). An upwind-biased conservative advection scheme for spherical hexagonal-pentagonal grids. *Monthly Weather Review*, *135*(12), 4038–4044. https://doi.org/10.1175/2007mwr2101.1

OpenFOAM. (2024). The OpenCFD Foundation. Retrieved from http://www.openfoam.org

Pareschi, L., & Russo, G. (2005). Implicit-explicit Runge-Kutta schemes and application to hyperbolic systems with relaxation. *Journal of Scientific Computing*, *25*(1/2), 129–155. https://doi.org/10.1007/bf02728986

Pudykiewicz, J., & Staniforth, A. (1984). Some properties and comparative performance of the semi-Lagrangian method of Robert in the solution of the advection-diffusion equation. *Atmosphere-Ocean*, *22*(3), 283–308. https://doi.org/10.1080/07055900.1984.9649200

Purser, R., & Leslie, L. (1991). An efficient interpolation procedure for high-order three-dimensional semi-Lagrangian models. *Monthly Weather Review*, *119*(10), 2492–2498. https://doi.org/10.1175/1520-0493(1991)119<2492:aeipfh>2.0.co;2

Putman, W., & Lin, S.-J. (2007). Finite-volume transport on various cubed-sphere grids. *Journal of Computational Physics*, *227*(1), 55–78. https://doi.org/10.1016/j.jcp.2007.07.022

Rang, J., & Angermann, L. (2005). New Rosenbrock W-methods of order 3 for partial differential algebraic equations of index 1. *BIT Numerical Mathematics*, *45*(4), 761–787. https://doi.org/10.1007/s10543-005-0035-y

Rhie, C., & Chow, W. (1983). Numerical study of the turbulent-flow past an airfoil with trailing edge separation. *AIAA Journal*, *21*(11), 1525–1532. https://doi.org/10.2514/3.8284

Robert, A. (1982). A semi-Lagrangian and semi-implicit numerical-integration scheme for the primitive meteorological equations. *Journal of the Meteorological Society of Japan*, *60*(1), 319–325. https://doi.org/10.2151/jmsj1965.60.1_319

Schär, C., Leuenberger, D., Fuhrer, O., Lüthi, D., & Girard, C. (2002). A new terrain-following vertical coordinate formulation for atmospheric prediction models. *Monthly Weather Review*, *130*(10), 2459–2480. https://doi.org/10.1175/1520-0493(2002)130<2459:antfvc>2.0.co;2

Shchepetkin, A. (2015). An adaptive, Courant-number-dependent implicit scheme for vertical advection in oceanic modeling. *Ocean Modelling*, *91*, 38–69. https://doi.org/10.1016/j.ocemod.2015.03.006

Shipley, D., Weller, H., Clark, P. A., & McIntyre, W. A. (2022). Two-fluid single-column modelling of Rayleigh-Bénard convection as a step towards multi-fluid modelling of atmospheric convection. *Quarterly Journal of the Royal Meteorological Society*, *148*(742), 351–377. https://doi.org/10.1002/qj.4209

Skamarock, W., & Menchaca, M. (2010). Conservative transport schemes for spherical geodesic grids: High-order reconstructions for forward-in-time schemes. *Monthly Weather Review*, *138*(12), 4497–4508. https://doi.org/10.1175/2010mwr3390.1

Smolarkiewicz, P., & Margolin, L. (1998). MPDATA: A finite-difference solver for geophysical flows. *Journal of Computational Physics*, *140*(2), 459–480. https://doi.org/10.1006/jcph.1998.5901

Smolarkiewicz, P., & Szmelter, J. (2005). MPDATA: An edge-based unstructured-grid formulation. *Journal of Computational Physics*, *206*(2), 624–649. https://doi.org/10.1016/j.jcp.2004.12.021

Smolarkiewicz, P. K., & Rasch, P. J. (1991). Monotone advection on the sphere: An Eulerian versus semi-Lagrangian approach. *Journal of the Atmospheric Sciences*, *48*(6), 793–810. https://doi.org/10.1175/1520-0469(1991)048<0793:maotsa>2.0.co;2

Weller, H. (2024a). The AtmosFOAM tools and applications for atmospheric modelling using OpenFOAM. https://doi.org/10.5281/zenodo.593780

Weller, H. (2024b). OpenFOAM test cases using AtmosFOAM. https://doi.org/10.5281/zenodo.11546593

Weller, H., Woodfield, J., Kühnlein, C., & Smolarkiewicz, P. K. (2023). Adaptively implicit MPDATA advection for arbitrary Courant numbers and meshes. *Quarterly Journal of the Royal Meteorological Society*, *149*(751), 369–388. https://doi.org/10.1002/qj.4411

Wicker, L., & Skamarock, W. (2020). An implicit-explicit vertical transport scheme for convection-allowing models. *Monthly Weather Review*, *148*(9), 3893–3910. https://doi.org/10.1175/mwr-d-20-0055.1

Yee, H. C., & Harten, A. (1987). Implicit TVD schemes for hyperbolic conservation laws in curvilinearcoordinates. *AIAA Journal*, *25*(2), 266–274. https://doi.org/10.2514/3.9617

Zalesak, S. (1979). Fully multidimensional flux-corrected transport algorithms for fluids. *Journal of Computational Physics*, *31*(3), 335–362. https://doi.org/10.1016/0021-9991(79)90051-2

Zerroukat, M., Wood, N., & Staniforth, A. (2004). SLICE-S: A semi-Lagrangian inherently conserving and efficient scheme for transport problems on the sphere. *Quarterly Journal of the Royal Meteorological Society*, *130*(602), 2649–2664. https://doi.org/10.1256/qj.03.200